A Defect in Influenza A Virus Particle Assembly Specific to Primary Human Macrophages

Sukhmani Bedi[a], Takeshi Noda[b], Yoshihiro Kawaoka[c,d], and Akira Ono[a]#

[a]Department of Microbiology and Immunology, University of Michigan Medical School, Ann Arbor, Michigan, USA

[b]Laboratory of Ultrastructural Virology, Department of Virus Research, Institute for Frontier Life and Medical Sciences, Kyoto University, Kyoto, Japan

[c]Division of Virology, Department of Microbiology and Immunology, Institute of Medical Science, University of Tokyo, Tokyo, Japan

[d]Department of Pathobiological Sciences, University of Wisconsin-Madison, Madison, Wisconsin, USA

Running title: Macrophage-specific Defect in Influenza Virus Assembly

Address correspondence to Akira Ono, Ph.D., akiraono@umich.edu

Word count for abstract: 250 (Abstract) and 149 (Importance)

Word count for text: 5,088

Abstract

The primary target of Influenza A virus (IAV) is epithelial cells in the respiratory tract. In contrast to epithelial cells, productive infection of most IAV strains is either blocked or highly inefficient in macrophages. The exact nature of the defect in IAV replication in human macrophages remains unknown. In this study, we showed that primary human monocyte-derived macrophages (MDM) are inefficient in IAV release even when compared to a monocytic cell line differentiated to macrophage-like cells, despite comparable levels of expression of viral glycoproteins at the plasma membrane. Correlative fluorescence scanning electron microscopy revealed that formation of budding structures at the cell surface is inefficient in MDM even though clustering of a viral glycoprotein, hemagglutinin (HA), is observed, suggesting that IAV particle assembly is blocked in human MDM. Using an *in situ* proximity ligation assay, we further determined that association between HA and the viral ion channel protein M2 is defective at the plasma membrane of MDM. In contrast, HA and another glycoprotein neuraminidase (NA) associate with each other on the MDM surface efficiently. Notably, the defect in association between HA and M2 in MDM was reversed upon inhibition of actin polymerization by cytochalasin D. Altogether, these results suggest that HA-M2 association on the plasma membrane is a discrete step in the IAV assembly process, which is separable from the association between HA and NA and susceptible to suppression by actin cytoskeleton. Overall, our study revealed the presence of a cell-type-specific mechanism negatively regulating IAV assembly at the plasma membrane.

Importance

Identification of host cell determinants promoting or suppressing replication of many viruses has been aided by analyses of host cells that impose inherent blocks on viral replication. In this study, we show that primary human MDM are not permissive to IAV replication due to a defect at the virus particle formation step. This defect is specific to primary human macrophages, since a human monocytic cell line differentiated to macrophage-like cells supports IAV particle formation. We further identified association between two viral transmembrane proteins, HA and M2, on the cell surface as a discrete assembly step, which is defective in MDM. Defective HA-M2 association in MDM is rescued by disruption of the actin cytoskeleton, revealing a previously unknown, negative role for actin polymerization, which is generally thought to play positive roles in IAV assembly. Overall, our study uncovered a host-mediated restriction of association between viral transmembrane components during IAV assembly.

60 **Introduction**

61 Influenza A virus (IAV) is a negative strand RNA virus that mainly infects
62 and replicates in epithelial cells in the respiratory tract. However, the virus has
63 also been shown to infect other cell types such as macrophages, dendritic cells,
64 and mast cells *ex vivo* (1-3). Host-cell-specific differences have been observed
65 for various properties of IAV including morphology and replication [for example,
66 (4-6)]. These differences could be due to differences in expression levels or
67 functions of host cellular proteins between cell types. In cases where cell-type-
68 specific differences affect productive infection of a virus, detailed comparison
69 between permissive and non-permissive cell types often leads to identification of
70 virus cofactors (5, 7-10) or host factors that restrict replication of viruses (6, 11-
71 14). This approach, which often determines the specific function of the host factor
72 of interest even prior to the identity of the factor, can serve as a complementary
73 approach to genome-wide approaches (15-24).

74 *Ex vivo* infection studies have shown that in comparison to epithelial cells,
75 murine and human macrophages are less permissive or non-permissive to
76 productive infection of seasonal IAV strains (25-31). In contrast to non-
77 permissive murine macrophages (25, 27, 31, 32), primary human blood-derived
78 or alveolar macrophages support seasonal IAV replication at detectable levels
79 although they are still much less permissive to virus growth than human epithelial
80 cells (26, 28, 29, 32). As for the defective stages of the IAV life cycle, a block at
81 the entry stage of infection has been identified in murine macrophages for most
82 H1N1 strains (25, 27, 31). In addition, the presence of a defect(s) at a later stage

83 has been known for IAV infection in murine macrophages (27, 31). However,
84 there are apparently conflicting data as to whether the defect is at pre- or post-
85 translation stage (27, 31). Moreover, the mechanism in either case has yet to be
86 determined. In contrast to murine macrophages, human macrophages support
87 early stages of replication of all tested IAV strains yet are unable to complete the
88 virus life cycle (31). While the defect appears to be post-translational, the exact
89 nature of this defect in human macrophages and the molecular mechanism
90 behind it are not known.

91 Determining the nature of the human macrophage-specific defect in IAV
92 replication is likely to advance our understanding of the roles played by cellular
93 functions in late phases of the IAV life cycle and potentially facilitate identification
94 of human host factors involved in this process. In the current study, we used
95 primary human monocyte-derived macrophages (MDM) in order to identify the
96 defective step in IAV replication in human macrophages. We show that MDM
97 support early stages of the IAV assembly process, i.e. trafficking of the viral
98 glycoproteins hemagglutinin (HA), neuraminidase (NA), and the ion channel
99 protein M2 to the plasma membrane, but are inefficient at virus particle formation
100 and subsequent virus release. This defect in virus particle formation and release
101 is specific to primary MDM, since a monocytic cell line THP1 differentiated into
102 macrophage-like cells supports efficient virus particle production. Notably, we
103 observed that the association of HA with M2 on the plasma membrane, as
104 determined by the close proximity of <40 nm, is highly inefficient in MDM relative
105 to the differentiated THP1 cells. In contrast, HA and NA associate efficiently on

the surface of MDM. The defective association between HA and M2 is rescued in MDM upon treatment with an actin polymerization inhibitor, cytochalasin D, whereas this defect is recreated in differentiated THP1 cells by treatment with jasplakinolide, which promotes actin polymerization. Overall, this study has identified virus particle formation, more specifically association between HA and M2, as the step defective in IAV life cycle in primary human macrophages and revealed that this host cell-specific block of IAV assembly requires actin polymerization.

116 **Results**

117 **MDM are inefficient in supporting productive IAV infection relative to**

118 **differentiated THP1 cells**

119 To determine the extent to which human epithelial cells and macrophages
120 differ in their ability to support productive IAV infection, we compared infectious
121 IAV release from three different human cell types: the lung-derived epithelial cell
122 line A549, the monocytic cell line THP1, which has been differentiated to adopt
123 macrophage-like morphology (dTHP1), and primary monocyte-derived
124 macrophages (MDM). The dTHP1 cells were obtained via treatment of THP1
125 cells with phorbol 12-myristate 13-acetate (PMA) and vitamin D3 for 2-3 days.
126 A549, dTHP1, and MDM were infected with the laboratory strain A/WSN/1933
127 (H1N1) (WSN) at MOI 0.01 based on the plaque forming units of virus stocks
128 determined using MDCK cells. At 11 hours post infection (hpi), we observed that
129 virus titers in MDM culture supernatants were up to 100-fold reduced in
130 comparison to that in A549 culture supernatants. Unexpectedly, virus titers in
131 culture supernatants were similar between A549 and dTHP1 cells (Figure 1A).
132 Since dTHP1 cells support influenza virus replication efficiently unlike MDM and
133 yet belong to the same cellular lineage, to facilitate the analyses of MDM-specific
134 defect(s), we chose to compare IAV replication in MDM with that in dTHP1 cells
135 in subsequent experiments. We noticed that while MDM isolated from the vast
136 majority of the tested human donors showed a defect in productive IAV infection
137 relative to dTHP1 at 24 hpi (denoted as Group 1 in Figure 1B), MDM from some
138 donors (denoted as Group 2 in Figure 1B; ~20%) showed no significant

139 difference. Therefore, to identify the MDM-specific defect, the subsequent
140 experiments were performed using MDM from the donors in Group 1. In
141 particular, in the mechanistic experiments (Figures 3-7), we verified in each
142 experiment that MDM used show 10-20 fold reduction in the supernatant virus
143 titers or released vRNA relative to dTHP1 cells at the indicated time point of the
144 corresponding assays (data not shown).
145 To assess whether other IAV strains also replicate inefficiently in MDM
146 relative to dTHP1 cells, we compared productive infection in dTHP1 cells and
147 MDM of three previously or currently circulating IAV strains, in addition to WSN:
148 A/Wyoming/03/2003 (H3N2) [Wyoming (H3N2)], A/Panama/2007/1999 (H3N2)
149 [Panama (H3N2)], and A/California/04/2009 (H1N1) [California (H1N1)].
150 Infectious virus titers of all tested IAV strains, as measured by the plaque assay,
151 were reduced by 10-50-fold in MDM in comparison to dTHP1 cells (Figure 1C).
152 These data suggest that MDM are highly inefficient at producing infectious IAV
153 particles in comparison to dTHP1 cells.
154
155 **Both efficiency of virus release and infectivity of released particles are**
156 **impaired in infected MDM relative to infected dTHP1 cells**
157 The results shown above and the results of time-course experiments
158 suggest that infectious virus release is reduced in MDM relative to dTHP1 cells
159 even though flow cytometry using anti-vRNP antibody (clone 61A5 (33)) showed
160 that similar fractions of cells in the cultures are infected (Figure 1 and
161 Supplementary Figure 1). We sought to address whether the reduction in viral

162 titers in MDM culture supernatants is due to a reduction in infectivity of released
163 particles or whether it is due to a reduction in release of physical particles. To this
164 end, we used viral RNA (vRNA) release as a surrogate to measure release of
165 physical particles from dTHP1 cells and MDM. Number of vRNA copies released
166 from MDM were 7-8-fold reduced in comparison to that from dTHP1 cells for all
167 eight vRNA segments. However, there were no significant decrease in cell-
168 associated vRNA levels in MDM relative to dTHP1 cells, indicating that MDM
169 support viral RNA replication and earlier steps as efficiently as dTHP1 cells.
170 vRNA release efficiency was calculated as the ratio of number of vRNA copies in
171 virus pellets from cell culture supernatants to the total number of vRNA copies
172 (cell + virus). For all eight vRNA segments, we observed a 5-10-fold reduction in
173 vRNA release efficiency in MDM relative to dTHP1 cells (Figure 2A). This
174 suggests that efficiency of physical viral particle release from MDM is reduced in
175 comparison to that from dTHP1 cells.
176 Importantly, the reduction in vRNA release (7-8-fold) from MDM does not
177 entirely account for reduction in infectious virus release (up to 50-fold) (Figure
178 2B). The ratio of released PFU (representing infectious virions) to released vRNA
179 (representing total number of particles) was calculated as the infectivity per
180 particle. Infectivity per particle for virus particles released from MDM was 5-6-fold
181 reduced versus that released from dTHP1 cells (Figure 2B). Overall, our data
182 suggest that the total number of virus particles released as well as the infectivity
183 of released virus particles is reduced in MDM relative to dTHP1 cells.
184

185 **Formation of budding structures is inefficient in MDM relative to dTHP1**
186 **cells despite similar levels of viral glycoprotein expression at the plasma**
187 **membrane**

188 We observed that total expression levels of vRNP, HA, and M1 are
189 comparable between dTHP1 cells and MDM (Supplementary Figures 1 and 2),
190 indicating that protein translation and earlier steps are unlikely to be impaired in
191 MDM. Henceforth, we focused on steps post viral protein translation: virus
192 assembly, budding and release. Virus assembly is initiated by targeting of the
193 glycoproteins HA and NA to the plasma membrane (34-36). The third
194 transmembrane protein M2 is also recruited to the assembly sites at the plasma
195 membrane and allows for completion of the virus budding process (35, 37). To
196 determine whether trafficking of the three glycoproteins occurs similarly in dTHP1
197 cells and MDM, we next compared levels of HA, NA and M2 proteins on the
198 surface of WSN-infected cells. We found that sizes of cell populations positive for
199 surface expression of the three proteins are comparable between MDM and
200 dTHP1 cells (Figures 3A and 3B). The mean fluorescence intensity (MFI) for the
201 three viral proteins in positive cell populations was also similar between MDM
202 and dTHP1 cells (Figure 3C), indicating that trafficking of viral glycoproteins to
203 the plasma membrane is comparable between MDM and dTHP1 cells.

204 We next asked whether dTHP1 cells and MDM expressing HA on the cell
205 surface support virus particle formation. To address this question in a single cell
206 basis, we performed correlative fluorescence and scanning electron microscopy
207 (CFSEM) in which we first identify cells with surface HA expression using

208 fluorescence microscopy and then examine formation of virus particle-like buds
209 on the surface of the same cells using scanning electron microscopy (SEM).
210 Fluorescence microscopy showed that HA is uniformly distributed on the surface
211 of both dTHP1 cells and MDM with some local accumulation. These HA-enriched
212 clusters or puncta, which likely represent sites of virus assembly, were clearly
213 distinguished on the surface of infected cells after the median filter was applied to
214 the confocal images to remove signal for uniformly distributed non-punctate HA.
215 These HA-enriched sites often corresponded to budding structures with a
216 diameter of approximately 100 nm on the surface of WSN-infected dTHP1 cells
217 (Figure 4A). Very few budding structures with the similar size were observed on
218 the surface of mock-infected cells. MDM also form ~100-nm virus particle-like
219 buds on the surface in HA-positive cells, albeit the number of buds observed in
220 MDM were markedly lower than in dTHP1 cells (Figure 4A). To assess the
221 formation of budding structures quantitatively, we counted the number of HA-
222 positive puncta and the number of virus particle-like buds within the same area
223 (100 μm^2 in size) of each cell. Even though MDM showed higher numbers of HA-
224 positive puncta on the cell surface than dTHP1 cells, the numbers of virus buds
225 were drastically reduced in MDM relative to dTHP1 cells (Figure 4B). Overall,
226 these results indicate that virus particle assembly/budding are inefficient in MDM
227 despite efficient trafficking of HA, NA and M2 to the plasma membrane.
228
229 **Association between HA and M2 is impaired in MDM but not in dTHP1 cells**

230 Based on results shown above, we hypothesize that local co-enrichment
231 of HA, NA and M2, which leads to formation of virus assembly sites, are not
232 efficient in MDM relative to dTHP1 cells. To compare formation of the putative
233 assembly sites between dTHP1 cells and MDM, we used *in situ* proximity ligation
234 assay (PLA). PLA allows for detection of two proteins localized within 40-nm
235 distance of each other and has been used to visualize IAV assembly sites on the
236 plasma membrane (38). In addition to measuring PLA signal between the given
237 pair of proteins, we also co-stained cells for cell surface NA to identify infected
238 cells. As a negative control, we performed PLA between HA and transferrin
239 receptor (TfR). TfR does not associate with lipid rafts (39), the plasma membrane
240 microdomains associated with IAV assembly sites (35, 40). Infected dTHP1 cells
241 showed high PLA signal for HA-M2 association. In contrast, infected MDM
242 showed very few PLA spots between HA and M2 (Figures 5A and 5C). As
243 expected, no PLA signal was observed between HA and M2 in mock-infected
244 cells or between HA and TfR in infected cells (Figure 5A). The majority (80-90%)
245 of surface NA-positive MDM and dTHP1 cells express HA and M2 on their
246 surface at comparable levels (Supplementary Figure 3). Therefore, the significant
247 reduction in HA-M2 PLA signal in MDM relative to dTHP1 cells is not due to the
248 lack of expression of HA and/or M2 in NA-positive cells.
249 To determine whether the defect in association between transmembrane
250 proteins in MDM is specific to HA and M2 or whether association between other
251 pairs of viral transmembrane proteins is defective as well, we next measured
252 PLA signal between HA and NA. In this case, to identify infected cells, we co-

253 stained cells for cell surface HA using an antibody different from the one used for
254 PLA. PLA signal between HA and NA was similar for dTHP1 cells and MDM,
255 suggesting that HA and NA associate with each other as efficiently on the
256 surface of MDM as on dTHP1 cells (Figures 5B and 5C). Overall, our data
257 indicate that association between HA and M2 is a virus assembly step
258 specifically impaired in MDM.
259
260 **Inhibition of actin polymerization restores HA-M2 PLA in MDM, while**
261 **promotion of actin polymerization reduces HA-M2 PLA in dTHP1 cells**
262 HA associates with lipid rafts on the plasma membrane, while M2 mainly
263 localizes in non-lipid raft areas (35, 40). It is suggested that M2 is recruited to
264 cholesterol-rich lipid rafts during IAV particle assembly (41, 42); however, host
265 cell functions and factors that regulate this step are not known. It is possible that
266 in MDM, HA-containing plasma membrane microdomains stay segregated from
267 those containing M2, leading to defective association between the two
268 glycoproteins. The cortical actin cytoskeleton, a network of filaments that
269 underlies and interacts with the plasma membrane, is suggested to play a role in
270 formation and maintenance of plasma membrane microdomains (43-45).
271 Therefore, we next asked whether the actin network regulates the association
272 between HA and M2 in dTHP1 cells and MDM. Infected cells were treated with
273 cytochalasin D (Cyto D), an inhibitor of actin polymerization, at 14 hpi for 2 hours,
274 fixed, and examined for HA-M2 association using PLA. Infected dTHP1 cells
275 showed high PLA signal for HA-M2 association under both untreated and Cyto D-

276 treated conditions. As observed in Figure 5B, untreated MDM showed very few
277 PLA spots between HA and M2. In contrast, Cyto D-treated MDM showed PLA
278 signal between HA and M2 at levels similar to that observed for dTHP1 cells
279 (Figures 6A and 6B). No PLA signal was observed between HA and TfR in
280 untreated or Cyto D-treated dTHP1 cells and MDM. The increase in HA-M2 PLA
281 signal upon Cyto D treatment of MDM was not due to an increase in surface
282 expression of HA and M2 in drug-treated cells, as shown by the flow cytometry
283 analysis (Supplementary Figure 4).

284 Since inhibition of actin polymerization restores association of HA and M2
285 in MDM, we next asked whether promoting actin polymerization inhibits HA-M2
286 association in dTHP1 cells. To this end, infected dTHP1 cells were treated with
287 jasplakinolide (Jasp), which nucleates and stabilizes actin polymerization, at 14
288 hpi for 2 hours and examined for HA-M2 association using PLA at 16 hpi as in
289 Figure 6. Two hours of Jasp treatment reduced HA-M2 PLA in 50% of the
290 examined dTHP1 cells, while the remaining infected cell population showed HA-
291 M2 PLA signal comparable to that in untreated cells (data not shown). We
292 reasoned that high HA-M2 PLA signal in 50% of Jasp-treated dTHP1 cells is due
293 to pre-existing association between HA and M2 at the time of Jasp addition.
294 Therefore, we next examined the effect of Jasp on HA-M2 association at an
295 earlier time point in infection when pre-existing HA-M2 coclusters are unlikely to
296 be abundant. We treated infected dTHP1 cells with Jasp or Cyto D at 10 hpi for 4
297 hours and examined for HA-M2 association using PLA at 14 hpi. Under these
298 conditions, most Jasp-treated dTHP1 cells showed reduced HA-M2 PLA signal,

299 in comparison to untreated or Cyto D-treated cells (Figures 7A and 7B). Since
300 the defect in HA-M2 association is rescued upon inhibition of actin polymerization
301 in MDM while it is induced upon stabilization of actin in dTHP1 cells, our data
302 overall highlight a role for actin polymerization in suppressing association
303 between HA and M2 at the plasma membrane.

304 **Discussion**

305 In a previous study, a post-translational defect in productive IAV infection
306 was observed in human MDM (31). A similar defect was also reported for murine
307 macrophages in one study (27) but not the other (31). The exact nature of these
308 defects that lead to inefficient IAV release has not been determined. Here, we
309 have shown that despite efficient trafficking of the viral glycoproteins to the cell
310 surface (Figure 3), infectious virus particle formation at the plasma membrane is
311 inefficient in human MDM (Figures 2 and 4). The current study further identified
312 HA-M2 association as an IAV assembly step suppressed in MDM (Figure 5). This
313 restriction is specific to primary macrophages, as the THP1 monocytic cell line
314 differentiated to macrophage-like cells (dTHP1 cells) support HA-M2 association
315 and efficient IAV production. Notably, defective HA-M2 association in MDM can
316 be reversed by the disruption of actin polymerization, suggesting a role for the
317 actin cytoskeleton in suppressing this step of IAV assembly in MDM (Figure 6).
318 Consistent with the restrictive role of actin polymerization, the HA-M2 association
319 in dTHP1 cells was blocked upon a treatment that promotes actin polymerization
320 (Figure 7).

321 Previous studies observed strain-specific differences for IAV replication in
322 human macrophages. Some strains such as highly pathogenic H5N1 and
323 pandemic 1918 strains can replicate in macrophages albeit at a lower efficiency
324 than in epithelial cells (25, 26, 29, 32). Marvin *et al.* recently reported that the
325 laboratory strain WSN is able to overcome blocks in IAV replication in human
326 macrophages, while replication of the A/California/04/2009 strain is completely

327 blocked (31). In our study, we observed that all tested strains, including WSN
328 and A/California/04/2009, released significantly lower titers in MDM than in
329 dTHP1 cells (Figure 1C). Thus, it is likely that the cell-type-specific difference
330 observed in this study is distinct from the previously reported strain-specific
331 difference.

332 In addition to identifying the defective step for IAV replication in primary
333 human macrophages, our study also lends mechanistic insights into the
334 assembly and budding process of IAV in host cells. IAV is thought to assemble in
335 cholesterol-enriched microdomains, or membrane rafts, of the plasma membrane
336 in host cells (46-49). HA and NA accumulate at these assembly sites (34-36, 40,
337 50), also known as the budozones, while the third transmembrane protein M2 is
338 suggested to localize at the edge of the budozone (37, 42, 51). Coclustering
339 between HA and M2 has been observed at steady state in epithelial cells (41, 51,
340 52). However, the sequence of events leading to recruitment of M2 to the
341 budozone is unknown. Whether there is a mechanism regulating these events,
342 other than simple diffusion over the plasma membrane, also remains to be
343 determined. Our PLA data suggest that association between HA and NA likely
344 precedes association between HA and M2. Consistent with this possibility, a
345 recent study showed that NA but not M2 accelerates HA trafficking to the apical
346 surface of epithelial cells, presumably through co-trafficking (50). Thus,
347 recruitment of M2 to assembly sites enriched in HA (and perhaps NA) is a
348 discrete and host-cell-dependent step in the IAV assembly process.

349 The actin cytoskeleton has been implicated in assembly of IAV particles,
350 in particular formation of filamentous particles (4, 53, 54). However, the actin-
351 dependent mechanism(s) regulating IAV assembly are not well understood.
352 Previous studies have shown that disruption of actin dynamics by both inhibition
353 of actin polymerization (4, 53) (by latrunculin A or cytochalasin D) and promotion
354 of actin polymerization (53) (by jasplakinolide) disrupts filamentous IAV
355 assembly. In contrast, our study showed that drugs inhibiting actin polymerization
356 and depolymerization have distinct and opposing effects on HA-M2 association:
357 blocking actin polymerization in IAV non-permissive cells (MDM) restores HA-M2
358 association, whereas enhancement of polymerization in permissive cells (dTHP1
359 cells) reduces HA-M2 association. Therefore, it is likely that distinct actin-
360 dependent mechanisms regulate the association between HA and M2 at the
361 plasma membrane and formation of filamentous particles. The regulation of HA-
362 M2 association may depend on the segregation of HA- and M2-enriched plasma
363 membrane microdomains by the actin cytoskeleton. Consistent with this
364 possibility, previous studies support a role for actin polymerization in maintaining
365 HA-enriched microdomains compact and dense (55, 56).
366 The cytoplasmic domain of M2 comprises of an amphipathic helix, which
367 plays a role in scission of the IAV particle after budding (37, 51). Previous studies
368 have described the role of M2 in assembly and scission of virus buds (51, 57),
369 vRNP incorporation (58-61), and M1 binding (41, 58, 61-63) using virus strains
370 that either lack M2 expression or express M2 cytoplasmic tail mutants.
371 Interestingly, in epithelial cells, virus lacking M2 or expressing mutant M2

372 proteins is still able to initiate particle assembly and budding, presumably
373 mediated by HA and NA (34, 64). However, these buds adopt an abnormal
374 morphology and/or fail to undergo scission or release (37, 51, 60), latter of which
375 results in accumulation of particles at the cell surface. In contrast, MDM showed
376 very few buds on their surface (Figure 4), suggesting that in MDM, an earlier role
377 for M2 in virus particle assembly is more prominent than in epithelial cells.
378 Consistent with this early role of M2 in IAV assembly, M2 functions in recruitment
379 of M1 and vRNP to assembly sites (41, 58-63), which is important for initiation of
380 IAV particle assembly or elongation of filamentous particles (58, 60, 65-71). A
381 defect in incorporation of M1 and/or vRNP into budding virus particles due to the
382 failure of M2 recruitment may also explain the reduction in infectivity per particle
383 observed for MDM-derived virus relative to dTHP1-derived virus (Figure 2B). We
384 also do not rule out the possibility that a failure in M1 association with the
385 assembly sites may contribute to the observed defect in M2-HA association
386 specific to MDM. However, we note that there was no major difference in
387 distribution of M1 relative to the site of HA accumulation at the plasma
388 membrane between MDM and dTHP1 cells (unpublished observations).
389 Overall, in this study, we have compared IAV replication in MDM with that
390 in dTHP1 cells and found that MDM replicate vRNA, express viral proteins, and
391 traffic HA, NA and M2 to the plasma membrane at levels similar to those in
392 dTHP1 cells. However, MDM are defective in assembling virus particles, likely
393 due to actin-dependent suppression of association between the viral
394 transmembrane proteins HA and M2. Comparison of actin regulatory

395 mechanisms operating in MDM and dTHP1 cells, which are of the same lineage,
396 will likely facilitate identification of additional host cellular factors involved in the
397 assembly stage of the IAV life cycle.
398
399

400 **Materials and Methods**

401 **Cells and reagents:** Monocytes were isolated by plate adhesion from peripheral
402 blood mononuclear cells, which were obtained from buffy coats derived from
403 unidentified healthy donors (New York Blood Center, NY). Cells were cultured in
404 RPMI 1640(Gibco) supplemented with 10% fetal bovine serum (FBS, Hyclone)
405 for 7 days before they were used for experiments. THP1 (ATCC® TIB202™)
406 cells were cultured in RPMI 1640 supplemented with 10% FBS, 1 mM Sodium
407 Pyruvate (Gibco) and 0.05 mM 2-mercaptoethanol. To generate differentiated
408 THP1 cells (dTHP1), THP1 cells were cultured in the medium containing 0.1 μM
409 phorbol 12-myristate 13-acetate (PMA; Sigma) and 0.1 μM Vitamin D3 (Sigma)
410 for 2-3 days. Madin-Darby canine kidney (MDCK) cells were provided by Dr.
411 Arnold S. Monto (University of Michigan) and were cultured in DMEM (Gibco)
412 supplemented with 10% FBS and 25 mM HEPES. Human lung carcinoma cell
413 line A549 was provided by Dr. Mike Bachman (University of Michigan) and was
414 cultured in DMEM (Gibco) supplemented with 10% FBS and 25 mM HEPES.
415 Human embryonic kidney-derived 293T cell line (ATCC) was cultured and
416 maintained in DMEM (Lonza) supplemented with 10% FBS.
417 The following antibodies were used for immunofluorescence microscopy: mouse
418 anti-HA monoclonal antibody (clone C179 (72); Takara), mouse anti-M2
419 monoclonal antibody (clone 14C2 (73); Thermofisher), mouse anti-vRNP
420 monoclonal antibody (clone 61A5 (33); a kind gift from Dr. Fumitaka Momose,
421 Kitasato University), goat anti-HA antiserum (BEI NR-3148), mouse anti-
422 transferrin receptor (TfR) monoclonal antibody (clone M-A712; BD Biosciences).

423 Rabbit anti-NA antiserum was a kind gift from Dr. Christopher Brooke (University
424 of Illinois). All secondary antibodies used for immunofluorescence were
425 purchased from Thermofisher. Cytochalasin D and Jasplakinolide were
426 purchased from Sigma and re-constituted in DMSO and 100% Ethanol,
427 respectively.
428
429 **Plasmids and virus stocks:** A/WSN/1933 (H1N1) virus was generated by
430 reverse genetics (74) using the 8 pPolI plasmids encoding different segments of
431 IAV genome and the 4 pCAGGS plasmids that express the PA, PB1, PB2, and
432 NP proteins. The titers of the stocks were determined using the plaque assay
433 with MDCK cells. A/Wyoming/03/2003 (H3N2) [Wyoming (H3N2)],
434 A/Panama/2007/1999 (H3N2) [Panama (H3N2)], and A/California/04/2009
435 (H1N1) [California (H1N1)] viruses were kind gifts from Dr. Arnold S. Monto
436 (University of Michigan) and were received as low passage stocks (less than 5
437 passages in MDCK cells) of virus isolated from clinical specimen. Virus infection
438 was performed and monitored using the plaque assay and flow cytometry as
439 described in Supplementary Information.
440
441 **Measurement of vRNA levels:** Virus-containing cell culture supernatants were
442 centrifuged at 3000 rpm for 5 minutes in a microfuge, filtered through a 0.45-μm
443 filter, and subjected to ultracentrifugation at 30,800 rpm (AH650 swinging bucket
444 rotor, Thermofisher) for 90 minutes to prepare virus pellets. Virus and cell-
445 associated vRNA was measured using a previously described protocol (75).

446 Briefly, total RNA was extracted from virus pellets and cell lysates using TRIzol
447 reagent (Ambion) according to the manufacturer's protocol. Complementary DNA
448 was generated using random hexamer priming and the SuperScript III First-
449 Strand Synthesis System (Invitrogen). Quantitative PCR was performed on a
450 CFX96 Real Time PCR system (Biorad) using Platinum SYBR Green pPCR
451 SuperMiX-UDG (Thermo Scientific Fisher). Serial ten-fold dilutions of pPolI
452 plasmids containing specific viral gene of WSN were used to generate a standard
453 curve for quantification of cDNA copy number based on cycle threshold (Ct)
454 values. The primer sequences are shown in Supplementary Information.
455
456 **Correlative fluorescence and scanning electron microscopy (CFSEM):**
457 CFSEM experiments were performed as described before (76). Briefly, cells
458 cultured on gridded coverslips (Bellco Biotechnology) were infected with WSN at
459 MOI 0.1. Cells were fixed with 4% PFA in PBS at 20 hpi. After rinsing in PBS,
460 quenching of PFA with PBS containing 0.1 M glycine (Sigma), and blocking with
461 PBS containing 3% bovine serum albumin (BSA, Sigma), cells were
462 immunostained with mouse anti-HA and fluorescently labeled secondary
463 antibody. Cells were imaged using a Leica Inverted SP5X Confocal Microscope
464 with a 40× PL APO objective and 10-20× scanning zoom. After fluorescence
465 imaging, cells were fixed with PBS containing 2.5% glutaraldehyde (Electron
466 Microscopy Sciences), stained with 1% OsO_4,dehydrated in a series of ethanol
467 washes, rinsed in hexamethyldisilazane (Electron Microscopy Sciences) and
468 allowed to dry overnight. Coverslips were affixed to specimen mounts and sputter

469 coated with gold for 90 s (Polaron). Cells were identified by their location on the
470 gridded coverslip and imaged on an Amray 1910FEG scanning electron
471 microscope at 5-10 kV. Fluorescence and SEM images were roughly brought into
472 registration by scaling and rotating images in Adobe Illustrator, similarly to other
473 correlative fluorescence/SEM studies (76). Landmarks used for registration
474 included cell edges. Cell surface structures visible in SEM were manually
475 classified as virus-like buds if they appeared spherical and near 100 nm in
476 diameter. To identify HA clusters in fluorescence images unambiguously, we
477 removed uniform non-puncta HA signal from the images. To do this, we
478 calculated a 20-pixel radius median filter and subtracted the median filtered
479 image from the original using the *Image Calculator* function in ImageJ. Number of
480 HA-positive puncta was measured in the background-subtracted fluorescence
481 images using the *Analyze particle* function in ImageJ. Since MDM have
482 substantial membrane folds on the cell surface especially towards the center of
483 the cell, we focused on areas towards the edge of the cells, which have a flatter
484 topology, for quantification of efficiency of virus bud formation.
485
486 ***In situ* Proximity Ligation Assay (PLA):** PLA was performed using
487 Duolink® PLA fluorescence kit following the manufacturer's instruction (Sigma).
488 Cells fixed with 4% PFA (non-permeabilized) were incubated with following
489 primary antibody combinations: goat anti-HA and mouse anti-M2 for PLA and
490 rabbit anti-NA for identification of infected cells; mouse anti-HA and rabbit anti-
491 NA for PLA and goat anti-HA for identification of infected cells; or goat anti-HA

492 and mouse anti-TfR for PLA and rabbit anti-NA for identification of infected cells.
493 Detection of PLA signals and identification of infected cells were performed using
494 PLA probes specific to goat, mouse or rabbit IgG and AlexaFluor-488-labeled
495 secondary antibody recognizing anti-NA or anti-HA, respectively. Cells were
496 observed using a Leica Inverted SP5X Confocal Microscope System with a 63X
497 objective. Z-stacks extending from the focal plane corresponding to the middle
498 plane of the nucleus (identified by DAPI staining) to the bottom of cells were
499 acquired for each cell, and the maximum intensity projection for each cell was
500 constructed using ImageJ. The PLA signal in projection images was thresholded
501 to eliminate weak and hazy background signal in the nucleus, and the number of
502 PLA-positive spots was counted using the *Analyze particle* function in ImageJ.
503
504 **Statistical analysis:** Statistical analyses were performed using GraphPad Prism
505 version 7. Two-tailed paired student *t* test was used to calculate p-values in
506 Figures 1-3 and supplementary Figures 1-4. Two-tailed unpaired student *t* test
507 was performed in Figures 4-7.
508

Acknowledgments

We would like to thank the members of our laboratories for helpful discussions and critical review of the manuscript. We would like to thank Drs. Bachman, Brooke, Momose, and Monto for reagents. The following reagent was obtained through BEI Resources, NIAID, NIH: Polyclonal Anti-Influenza Virus H1 (H0) Hemagglutinin (HA), A/Puerto Rico/8/1934 (H1N1), (antiserum, Goat), NR-3148. This work was supported by funding from the National Institutes of Health (R01 AI071727) (to A.O), the Takeda Science Foundation (to T.N), and Leading Advanced Projects for medical innovation (LEAP) from the Japan Agency for Medical Research and Development (AMED) (JP17am0001007) (to Y.K.). S.B. was supported by a Clayton Willison- and Emma Elizabeth Willison-Endowed Graduate Fellowship.

523 **References:**

524 1. **Rodgers BC, Mims CA.** 1982. Influenza virus replication in human
525 alveolar macrophages. J Med Virol **9:**177-184.

526 2. **Hartmann BM, Li W, Jia J, Patil S, Marjanovic N, Martínez-Romero C,**
527 **Albrecht RA, Hayot F, García-Sastre A, Wetmur JG, Moran TM,**
528 **Sealfon SC.** 2013. Mouse dendritic cell (DC) influenza virus infectivity is
529 much lower than that for human DCs and is hemagglutinin subtype
530 dependent. J Virol **87:**1916-1918.

531 3. **Graham AC, Hilmer KM, Zickovich JM, Obar JJ.** 2013. Inflammatory
532 response of mast cells during influenza A virus infection is mediated by
533 active infection and RIG-I signaling. J Immunol **190:**4676-4684.

534 4. **Roberts PC, Compans RW.** 1998. Host cell dependence of viral
535 morphology. Proc Natl Acad Sci U S A **95:**5746-5751.

536 5. **Moncorgé O, Mura M, Barclay WS.** 2010. Evidence for avian and human
537 host cell factors that affect the activity of influenza virus polymerase. J
538 Virol **84:**9978-9986.

539 6. **Mehle A, Doudna JA.** 2008. An inhibitory activity in human cells restricts
540 the function of an avian-like influenza virus polymerase. Cell Host Microbe
541 **4:**111-122.

542 7. **Feng Y, Broder CC, Kennedy PE, Berger EA.** 1996. HIV-1 entry
543 cofactor: functional cDNA cloning of a seven-transmembrane, G protein-
544 coupled receptor. Science **272:**872-877.

545 8. **Bortz E, Westera L, Maamary J, Steel J, Albrecht RA, Manicassamy**
546 **B, Chase G, Martínez-Sobrido L, Schwemmle M, García-Sastre A.**
547 2011. Host- and strain-specific regulation of influenza virus polymerase
548 activity by interacting cellular proteins. MBio **2**.
549 9. **Hudjetz B, Gabriel G.** 2012. Human-like PB2 627K influenza virus
550 polymerase activity is regulated by importin-α1 and -α7. PLoS Pathog
551 **8:**e1002488.
552 10. **Long JS, Giotis ES, Moncorgé O, Frise R, Mistry B, James J,**
553 **Morisson M, Iqbal M, Vignal A, Skinner MA, Barclay WS.** 2016.
554 Species difference in ANP32A underlies influenza A virus polymerase host
555 restriction. Nature **529:**101-104.
556 11. **Kuo SM, Chen CJ, Chang SC, Liu TJ, Chen YH, Huang SY, Shih SR.**
557 2017. Inhibition of Avian Influenza A Virus Replication in Human Cells by
558 Host Restriction Factor TUFM Is Correlated with Autophagy. MBio **8**.
559 12. **Laguette N, Sobhian B, Casartelli N, Ringeard M, Chable-Bessia C,**
560 **Ségéral E, Yatim A, Emiliani S, Schwartz O, Benkirane M.** 2011.
561 SAMHD1 is the dendritic- and myeloid-cell-specific HIV-1 restriction factor
562 counteracted by Vpx. Nature **474:**654-657.
563 13. **Neil SJ, Zang T, Bieniasz PD.** 2008. Tetherin inhibits retrovirus release
564 and is antagonized by HIV-1 Vpu. Nature **451:**425-430.
565 14. **Sheehy AM, Gaddis NC, Choi JD, Malim MH.** 2002. Isolation of a human
566 gene that inhibits HIV-1 infection and is suppressed by the viral Vif protein.
567 Nature **418:**646-650.

568 15. **Hao L, Sakurai A, Watanabe T, Sorensen E, Nidom CA, Newton MA,**
569 **Ahlquist P, Kawaoka Y.** 2008. Drosophila RNAi screen identifies host
570 genes important for influenza virus replication. Nature **454:**890-893.
571 16. **Shapira SD, Gat-Viks I, Shum BO, Dricot A, de Grace MM, Wu L,**
572 **Gupta PB, Hao T, Silver SJ, Root DE, Hill DE, Regev A, Hacohen N.**
573 2009. A physical and regulatory map of host-influenza interactions reveals
574 pathways in H1N1 infection. Cell **139:**1255-1267.
575 17. **Karlas A, Machuy N, Shin Y, Pleissner KP, Artarini A, Heuer D,**
576 **Becker D, Khalil H, Ogilvie LA, Hess S, Mäurer AP, Müller E, Wolff T,**
577 **Rudel T, Meyer TF.** 2010. Genome-wide RNAi screen identifies human
578 host factors crucial for influenza virus replication. Nature **463:**818-822.
579 18. **König R, Stertz S, Zhou Y, Inoue A, Hoffmann HH, Bhattacharyya S,**
580 **Alamares JG, Tscherne DM, Ortigoza MB, Liang Y, Gao Q, Andrews**
581 **SE, Bandyopadhyay S, De Jesus P, Tu BP, Pache L, Shih C, Orth A,**
582 **Bonamy G, Miraglia L, Ideker T, García-Sastre A, Young JA, Palese P,**
583 **Shaw ML, Chanda SK.** 2010. Human host factors required for influenza
584 virus replication. Nature **463:**813-817.
585 19. **Su WC, Chen YC, Tseng CH, Hsu PW, Tung KF, Jeng KS, Lai MM.**
586 2013. Pooled RNAi screen identifies ubiquitin ligase Itch as crucial for
587 influenza A virus release from the endosome during virus entry. Proc Natl
588 Acad Sci U S A **110:**17516-17521.
589 20. **Watanabe T, Kawakami E, Shoemaker JE, Lopes TJ, Matsuoka Y,**
590 **Tomita Y, Kozuka-Hata H, Gorai T, Kuwahara T, Takeda E, Nagata A,**

591 **Takano R, Kiso M, Yamashita M, Sakai-Tagawa Y, Katsura H, Nonaka**
592 **N, Fujii H, Fujii K, Sugita Y, Noda T, Goto H, Fukuyama S, Watanabe**
593 **S, Neumann G, Oyama M, Kitano H, Kawaoka Y.** 2014. Influenza virus-
594 host interactome screen as a platform for antiviral drug development. Cell
595 Host Microbe **16:**795-805.
596 21. **Tripathi S, Pohl MO, Zhou Y, Rodriguez-Frandsen A, Wang G, Stein**
597 **DA, Moulton HM, DeJesus P, Che J, Mulder LC, Yángüez E,**
598 **Andenmatten D, Pache L, Manicassamy B, Albrecht RA, Gonzalez**
599 **MG, Nguyen Q, Brass A, Elledge S, White M, Shapira S, Hacohen N,**
600 **Karlas A, Meyer TF, Shales M, Gatorano A, Johnson JR, Jang G,**
601 **Johnson T, Verschueren E, Sanders D, Krogan N, Shaw M, König R,**
602 **Stertz S, García-Sastre A, Chanda SK.** 2015. Meta- and Orthogonal
603 Integration of Influenza "OMICs" Data Defines a Role for UBR4 in Virus
604 Budding. Cell Host Microbe **18:**723-735.
605 22. **Meliopoulos VA, Andersen LE, Birrer KF, Simpson KJ, Lowenthal**
606 **JW, Bean AG, Stambas J, Stewart CR, Tompkins SM, van Beusechem**
607 **VW, Fraser I, Mhlanga M, Barichievy S, Smith Q, Leake D, Karpilow J,**
608 **Buck A, Jona G, Tripp RA.** 2012. Host gene targets for novel influenza
609 therapies elucidated by high-throughput RNA interference screens.
610 FASEB J **26:**1372-1386.
611 23. **Heaton NS, Moshkina N, Fenouil R, Gardner TJ, Aguirre S, Shah PS,**
612 **Zhao N, Manganaro L, Hultquist JF, Noel J, Sachs D, Hamilton J,**
613 **Leon PE, Chawdury A, Tripathi S, Melegari C, Campisi L, Hai R,**

614 **Metreveli G, Gamarnik AV, García-Sastre A, Greenbaum B, Simon V,**
615 **Fernandez-Sesma A, Krogan NJ, Mulder LCF, van Bakel H, Tortorella**
616 **D, Taunton J, Palese P, Marazzi I.** 2016. Targeting Viral Proteostasis
617 Limits Influenza Virus, HIV, and Dengue Virus Infection. Immunity **44:**46-
618 58.
619 24. **Heaton BE, Kennedy EM, Dumm RE, Harding AT, Sacco MT, Sachs D,**
620 **Heaton NS.** 2017. A CRISPR Activation Screen Identifies a Pan-avian
621 Influenza Virus Inhibitory Host Factor. Cell Rep **20:**1503-1512.
622 25. **Cline TD, Karlsson EA, Seufzer BJ, Schultz-Cherry S.** 2013. The
623 hemagglutinin protein of highly pathogenic H5N1 influenza viruses
624 overcomes an early block in the replication cycle to promote productive
625 replication in macrophages. J Virol **87:**1411-1419.
626 26. **Yu WC, Chan RW, Wang J, Travanty EA, Nicholls JM, Peiris JS,**
627 **Mason RJ, Chan MC.** 2011. Viral replication and innate host responses in
628 primary human alveolar epithelial cells and alveolar macrophages infected
629 with influenza H5N1 and H1N1 viruses. J Virol **85:**6844-6855.
630 27. **Londrigan SL, Short KR, Ma J, Gillespie L, Rockman SP, Brooks AG,**
631 **Reading PC.** 2015. Infection of Mouse Macrophages by Seasonal
632 Influenza Viruses Can Be Restricted at the Level of Virus Entry and at a
633 Late Stage in the Virus Life Cycle. J Virol **89:**12319-12329.
634 28. **Mok CK, Lee DC, Cheung CY, Peiris M, Lau AS.** 2007. Differential onset
635 of apoptosis in influenza A virus H5N1- and H1N1-infected human blood
636 macrophages. J Gen Virol **88:**1275-1280.

637 29. **Sakabe S, Iwatsuki-Horimoto K, Takano R, Nidom CA, Le M,**
638 **Nagamura-Inoue T, Horimoto T, Yamashita N, Kawaoka Y.** 2011.
639 Cytokine production by primary human macrophages infected with highly
640 pathogenic H5N1 or pandemic H1N1 2009 influenza viruses. J Gen Virol
641 **92:**1428-1434.
642 30. **van Riel D, Leijten LM, van der Eerden M, Hoogsteden HC, Boven LA,**
643 **Lambrecht BN, Osterhaus AD, Kuiken T.** 2011. Highly pathogenic avian
644 influenza virus H5N1 infects alveolar macrophages without virus
645 production or excessive TNF-alpha induction. PLoS Pathog **7:**e1002099.
646 31. **Marvin SA, Russier M, Huerta CT, Russell CJ, Schultz-Cherry S.** 2016.
647 Influenza overcomes cellular blocks to productively replicate impacting
648 macrophage function. J Virol.
649 32. **Perrone LA, Plowden JK, García-Sastre A, Katz JM, Tumpey TM.**
650 2008. H5N1 and 1918 pandemic influenza virus infection results in early
651 and excessive infiltration of macrophages and neutrophils in the lungs of
652 mice. PLoS Pathog **4:**e1000115.
653 33. **Momose F, Kikuchi Y, Komase K, Morikawa Y.** 2007. Visualization of
654 microtubule-mediated transport of influenza viral progeny
655 ribonucleoprotein. Microbes Infect **9:**1422-1433.
656 34. **Chen BJ, Leser GP, Morita E, Lamb RA.** 2007. Influenza virus
657 hemagglutinin and neuraminidase, but not the matrix protein, are required
658 for assembly and budding of plasmid-derived virus-like particles. J Virol
659 **81:**7111-7123.

660 35. **Leser GP, Lamb RA.** 2005. Influenza virus assembly and budding in raft-
661 derived microdomains: a quantitative analysis of the surface distribution of
662 HA, NA and M2 proteins. Virology **342:**215-227.
663 36. **Takeda M, Leser GP, Russell CJ, Lamb RA.** 2003. Influenza virus
664 hemagglutinin concentrates in lipid raft microdomains for efficient viral
665 fusion. Proc Natl Acad Sci U S A **100:**14610-14617.
666 37. **Rossman JS, Jing X, Leser GP, Lamb RA.** 2010. Influenza virus M2
667 protein mediates ESCRT-independent membrane scission. Cell **142:**902-
668 913.
669 38. **Kawaguchi A, Hirohama M, Harada Y, Osari S, Nagata K.** 2015.
670 Influenza Virus Induces Cholesterol-Enriched Endocytic Recycling
671 Compartments for Budozone Formation via Cell Cycle-Independent
672 Centrosome Maturation. PLoS Pathog **11:**e1005284.
673 39. **Harder T, Scheiffele P, Verkade P, Simons K.** 1998. Lipid domain
674 structure of the plasma membrane revealed by patching of membrane
675 components. J Cell Biol **141:**929-942.
676 40. **Zhang J, Pekosz A, Lamb RA.** 2000. Influenza virus assembly and lipid
677 raft microdomains: a role for the cytoplasmic tails of the spike
678 glycoproteins. J Virol **74:**4634-4644.
679 41. **Chen BJ, Leser GP, Jackson D, Lamb RA.** 2008. The influenza virus M2
680 protein cytoplasmic tail interacts with the M1 protein and influences virus
681 assembly at the site of virus budding. J Virol **82:**10059-10070.

682 42. **Rossman JS, Jing X, Leser GP, Balannik V, Pinto LH, Lamb RA.** 2010.
683 Influenza virus m2 ion channel protein is necessary for filamentous virion
684 formation. J Virol **84:**5078-5088.
685 43. **Liu AP, Fletcher DA.** 2006. Actin polymerization serves as a membrane
686 domain switch in model lipid bilayers. Biophys J **91:**4064-4070.
687 44. **Gaus K, Chklovskaia E, Fazekas de St Groth B, Jessup W, Harder T.**
688 2005. Condensation of the plasma membrane at the site of T lymphocyte
689 activation. J Cell Biol **171:**121-131.
690 45. **Chichili GR, Rodgers W.** 2007. Clustering of membrane raft proteins by
691 the actin cytoskeleton. J Biol Chem **282:**36682-36691.
692 46. **Schmitt AP, Lamb RA.** 2005. Influenza virus assembly and budding at
693 the viral budozone. Adv Virus Res **64:**383-416.
694 47. **Veit M, Thaa B.** 2011. Association of influenza virus proteins with
695 membrane rafts. Adv Virol **2011:**370606.
696 48. **Rossman JS, Lamb RA.** 2011. Influenza virus assembly and budding.
697 Virology **411:**229-236.
698 49. **Nayak DP, Balogun RA, Yamada H, Zhou ZH, Barman S.** 2009.
699 Influenza virus morphogenesis and budding. Virus Res **143:**147-161.
700 50. **Ohkura T, Momose F, Ichikawa R, Takeuchi K, Morikawa Y.** 2014.
701 Influenza A virus hemagglutinin and neuraminidase mutually accelerate
702 their apical targeting through clustering of lipid rafts. J Virol **88:**10039-
703 10055.

704 51. **Roberts KL, Leser GP, Ma C, Lamb RA.** 2013. The amphipathic helix of
705 influenza A virus M2 protein is required for filamentous bud formation and
706 scission of filamentous and spherical particles. J Virol **87:**9973-9982.
707 52. **Leser GP, Lamb RA.** 2017. Lateral Organization of Influenza Virus
708 Proteins in the Budozone Region of the Plasma Membrane. J Virol **91**.
709 53. **Simpson-Holley M, Ellis D, Fisher D, Elton D, McCauley J, Digard P.**
710 2002. A functional link between the actin cytoskeleton and lipid rafts
711 during budding of filamentous influenza virions. Virology **301:**212-225.
712 54. **Kumakura M, Kawaguchi A, Nagata K.** 2015. Actin-myosin network is
713 required for proper assembly of influenza virus particles. Virology
714 **476:**141-150.
715 55. **Gunewardene MS, Subach FV, Gould TJ, Penoncello GP, Gudheti**
716 **MV, Verkhusha VV, Hess ST.** 2011. Superresolution imaging of multiple
717 fluorescent proteins with highly overlapping emission spectra in living
718 cells. Biophys J **101:**1522-1528.
719 56. **Gudheti MV, Curthoys NM, Gould TJ, Kim D, Gunewardene MS,**
720 **Gabor KA, Gosse JA, Kim CH, Zimmerberg J, Hess ST.** 2013. Actin
721 mediates the nanoscale membrane organization of the clustered
722 membrane protein influenza hemagglutinin. Biophys J **104:**2182-2192.
723 57. **Martyna A, Bahsoun B, Badham MD, Srinivasan S, Howard MJ,**
724 **Rossman JS.** 2017. Membrane remodeling by the M2 amphipathic helix
725 drives influenza virus membrane scission. Sci Rep **7:**44695.

726 58. **Grantham ML, Stewart SM, Lalime EN, Pekosz A.** 2010. Tyrosines in
727 the influenza A virus M2 protein cytoplasmic tail are critical for production
728 of infectious virus particles. J Virol **84:**8765-8776.
729 59. **McCown MF, Pekosz A.** 2005. The influenza A virus M2 cytoplasmic tail
730 is required for infectious virus production and efficient genome packaging.
731 J Virol **79:**3595-3605.
732 60. **Iwatsuki-Horimoto K, Horimoto T, Noda T, Kiso M, Maeda J,**
733 **Watanabe S, Muramoto Y, Fujii K, Kawaoka Y.** 2006. The cytoplasmic
734 tail of the influenza A virus M2 protein plays a role in viral assembly. J
735 Virol **80:**5233-5240.
736 61. **Su WC, Yu WY, Huang SH, Lai MMC.** 2017. Ubiquitination of the
737 Cytoplasmic Domain of Influenza A Virus M2 Protein is Crucial for
738 Production of Infectious Virus Particles. J Virol.
739 62. **McCown MF, Pekosz A.** 2006. Distinct domains of the influenza a virus
740 M2 protein cytoplasmic tail mediate binding to the M1 protein and facilitate
741 infectious virus production. J Virol **80:**8178-8189.
742 63. **Wang D, Harmon A, Jin J, Francis DH, Christopher-Hennings J,**
743 **Nelson E, Montelaro RC, Li F.** 2010. The lack of an inherent membrane
744 targeting signal is responsible for the failure of the matrix (M1) protein of
745 influenza A virus to bud into virus-like particles. J Virol **84:**4673-4681.
746 64. **Chlanda P, Schraidt O, Kummer S, Riches J, Oberwinkler H, Prinz S,**
747 **Kräusslich HG, Briggs JA.** 2015. Structural Analysis of the Roles of

748 Influenza A Virus Membrane-Associated Proteins in Assembly and
749 Morphology. J Virol **89:**8957-8966.
750 65. **Burleigh LM, Calder LJ, Skehel JJ, Steinhauer DA.** 2005. Influenza a
751 viruses with mutations in the m1 helix six domain display a wide variety of
752 morphological phenotypes. J Virol **79:**1262-1270.
753 66. **Amorim MJ, Bruce EA, Read EK, Foeglein A, Mahen R, Stuart AD,**
754 **Digard P.** 2011. A Rab11- and microtubule-dependent mechanism for
755 cytoplasmic transport of influenza A virus viral RNA. J Virol **85:**4143-4156.
756 67. **Bourmakina SV, García-Sastre A.** 2005. The morphology and
757 composition of influenza A virus particles are not affected by low levels of
758 M1 and M2 proteins in infected cells. J Virol **79:**7926-7932.
759 68. **Moreira É, Weber A, Bolte H, Kolesnikova L, Giese S, Lakdawala S,**
760 **Beer M, Zimmer G, García-Sastre A, Schwemmle M, Juozapaitis M.**
761 2016. A conserved influenza A virus nucleoprotein code controls specific
762 viral genome packaging. Nat Commun **7:**12861.
763 69. **Elleman CJ, Barclay WS.** 2004. The M1 matrix protein controls the
764 filamentous phenotype of influenza A virus. Virology **321:**144-153.
765 70. **Roberts PC, Lamb RA, Compans RW.** 1998. The M1 and M2 proteins of
766 influenza A virus are important determinants in filamentous particle
767 formation. Virology **240:**127-137.
768 71. **Liu H, Grantham ML, Pekosz A.** 2018. Mutations in the Influenza A Virus
769 M1 Protein Enhance Virus Budding To Complement Lethal Mutations in
770 the M2 Cytoplasmic Tail. J Virol **92**.

771 72. **Okuno Y, Isegawa Y, Sasao F, Ueda S.** 1993. A common neutralizing
772 epitope conserved between the hemagglutinins of influenza A virus H1
773 and H2 strains. J Virol **67:**2552-2558.
774 73. **Zebedee SL, Lamb RA.** 1988. Influenza A virus M2 protein: monoclonal
775 antibody restriction of virus growth and detection of M2 in virions. J Virol
776 **62:**2762-2772.
777 74. **Neumann G, Watanabe T, Ito H, Watanabe S, Goto H, Gao P, Hughes**
778 **M, Perez DR, Donis R, Hoffmann E, Hobom G, Kawaoka Y.** 1999.
779 Generation of influenza A viruses entirely from cloned cDNAs. Proc Natl
780 Acad Sci U S A **96:**9345-9350.
781 75. **Pauly MD, Lauring AS.** 2015. Effective lethal mutagenesis of influenza
782 virus by three nucleoside analogs. J Virol **89:**3584-3597.
783 76. **Hogue IB, Grover JR, Soheilian F, Nagashima K, Ono A.** 2011. Gag
784 induces the coalescence of clustered lipid rafts and tetraspanin-enriched
785 microdomains at HIV-1 assembly sites on the plasma membrane. J Virol
786 **85:**9749-9766.
787
788
789
790
791
792
793

797 **Figure legend:**

798

799 **Figure 1: MDM are defective in productive IAV infection.** (A) A549 cells,
800 dTHP1 cells and MDM were infected with WSN at MOI 0.01. Infectious virus
801 titers in culture supernatants were measured at 11 hpi. (B) Infectious virus titers
802 in culture supernatants were measured for WSN-infected dTHP1 cells and MDM
803 at 24 hpi. For all tested donors, the relative virus titers in MDM cultures were
804 calculated in comparison to the titer in dTHP1 cell cultures tested in parallel
805 within the same experiment. Two groups of donors (Groups 1 and 2) were
806 denoted based on the reduction in the titers or lack thereof. (C) dTHP1 and MDM
807 (Group 1) were infected with the given IAV strains at MOI 0.01, and infectious
808 virus titers in culture supernatants were measured at 24 hpi. Each circle
809 represents an independently prepared culture. A black and a red circle
810 connected by a line represent each independent experiment. For panel A, data
811 are shown as mean +/- SD. *, P<0.05; ***, P<0.001; ****, P<0.0001; ns, non-
812 significant.

813

814 **Figure 2: Both efficiency of virus release and infectivity of released**
815 **particles are reduced in MDM than in dTHP1 cells.** dTHP1 cells and
816 MDM were infected with WSN at MOI 0.1. (A) vRNA copy numbers were
817 measured in lysates of virus pelleted from cell culture supernatants and cell
818 lysates at 20 hpi. vRNA release efficiency was calculated as the ratio of number
819 of vRNA copies in virus lysates versus total number of vRNA copies (cell + virus)

820 for each vRNA segment. (B) PB2 vRNA copy number and virus titer were
821 measured in dTHP1 and MDM culture supernatants at 16 hpi. Infectivity per
822 particle was calculated as the ratio of virus titer to PB2 vRNA copy number in
823 culture supernatants. Data are from experiments done with MDM from at least
824 three independent donors and shown as mean +/- S.D. **, P<0.01; ***, P<0.001,
825 ****, P<0.0001.
826
827 **Figure 3: MDM are efficient at trafficking of viral glycoproteins to the cell**
828 **surface.** dTHP1 cells and MDM were infected with WSN at MOI 0.1. (A) Infected
829 cells were analyzed for cell surface expression of HA, NA, and M2 by flow
830 cytometry at 16 hpi. Representative flow plots for mock-infected (top row) and
831 virus-infected (bottom row) cells are shown. Percentages of cells positive for viral
832 proteins (boxed) are shown. Due to differences in the side scatter (SSC) profile
833 between dTHP1 cells and MDM, the Y-axis (SSC) range is different between the
834 two cell types. (B) Percentages of cells positive for surface expression of NA, HA,
835 and M2 are compared between dTHP1 and MDM. (C) Relative MFIs for surface
836 signal of indicated proteins for positive cell populations (gated in panel A) are
837 shown. Data are shown as mean +/- SD and are from at least three independent
838 experiments. ns, non-significant.
839
840 **Figure 4: MDM are defective in virus bud formation despite expression of**
841 **HA on the cell surface.** dTHP1 cells and MDM grown on gridded coverslips
842 were infected with WSN at MOI 0.1 for 20 hours. Cells were fixed and

843 immunostained with anti-HA. After identification of HA-positive cells by confocal
844 microscopy, cells were prepared for SEM. The same cells were identified based
845 on grid positions and analyzed by SEM. (A) Representative SEM images for
846 mock-infected and WSN-infected HA-positive cells are shown in the top and
847 bottom rows, respectively. Fluorescence images corresponding to the SEM
848 images of WSN-infected cells are shown in the middle row. Boxed areas are
849 magnified and shown in the right panels. (B) The number of HA-positive puncta
850 identified in fluorescence images (left panel) and ~100-nm buds identified in SEM
851 images (right panel) were counted within the same area (100 μm^2 in size) in each
852 cell. Data are shown for 8-15 cells from two independent experiments. Error bars
853 represent SEM. ***, P<0.0001; ns, non-significant.
854
855 **Figure 5: Association between HA and M2 is defective in MDM relative to**
856 **dTHP1 cells.** dTHP1 cells and MDM were infected with WSN at MOI 0.1 for 16
857 hours. (A) Cells were examined by PLA using goat anti-HA and mouse anti-M2 or
858 goat anti-HA and mouse anti-TfR antibodies. To identify infected cells, surface
859 NA was also detected by rabbit anti-NA. Nuclei were stained with DAPI (blue).
860 Representative maximum intensity projection images, which were reconstructed
861 from z-stacks corresponding to the focal planes ranging from the middle plane of
862 the nucleus to the bottom of the cells, are shown. (B) Cells were examined by
863 PLA using mouse anti-HA and rabbit anti-NA antibodies. Goat anti-HA was used
864 for detection of infected cells. Representative maximum intensity projection
865 images are shown as in panel A. Note regions of intense NA (in A) and HA (in B)

866 signal on the surface of MDM due to the presence of membrane ruffles. (C)
867 Number of PLA spots were counted for each cell. Data are shown for three
868 independent experiments, and 8-10 cells were analyzed per experiment. These
869 experiments were performed in parallel with the experiments shown in Figure 3
870 using MDM from the same donors. Error bars represent SEM. *, $p<0.05$; ****, p
871 <0.0001; ns, non-significant.
872
873 **Figure 6: Cytochalasin D treatment restores HA-M2 PLA in MDM to levels**
874 **comparable to that in dTHP1 cells.** dTHP1 cells and MDM were infected with
875 WSN at MOI 0.1. At 14 hpi, cells were treated with vehicle control (DMSO) or 20
876 μM cytochalasin D (Cyto D) for 2 hours before fixation. (A) Cells were analyzed
877 as in Figure 5A. Representative maximum intensity projection images are shown.
878 (B) Number of PLA spots were counted for each cell. These experiments were
879 performed in parallel with the experiments shown in Supplementary Figure 4
880 using MDMs from the same donors. Data are from at least three independent
881 experiments, and 8-10 cells were analyzed per experiment. Error bars represent
882 SEM. ****, $p<0.0001$; ns, non-significant.
883
884 **Figure 7: Jasplakinolide treatment reduces HA-M2 PLA in dTHP1 cells.**
885 dTHP1 cells were infected with WSN at MOI 0.1. At 10 hpi, cells were treated
886 with vehicle control (100% Ethanol), 1 μM Jasplakinolide (Jasp), or 20 μM Cyto D
887 for 4 hours before fixation. (A) Representative maximum intensity projection
888 images are shown as in Figure 5A. (B) Number of PLA spots were counted for

889 each cell. Data are from at least three independent experiments, and 7-10 cells
890 were analyzed per experiment. Error bars represent SEM. *, $p < 0.05$; ns, non-
891 significant.
892
893

894 **Supplementary Information**

895

896 **Supplementary Figure 1: Infectious virus release is reduced in MDM**
897 **cultures relative to dTHP1 cells despite similar number of infected cells in**
898 **both cultures.** dTHP1 cells and MDM were infected with given IAV strains at
899 MOI 0.01. At the indicated time points post infection, culture supernatants and
900 cells were collected and assessed for virus titer (top panels) and % vRNP+ cells
901 (lower panels), respectively. Data from at least three independent experiments
902 are shown as mean +/- SD. *, P<0.05; **, P<0.01.

903

904 **Supplementary Figure 2: MDM express viral proteins as efficiently as**
905 **dTHP1 cells.** dTHP1 cells and MDM were infected with WSN at MOI 0.01 for 24
906 hours. Infected cells were fixed, permeabilized and analyzed for cellular levels of
907 vRNP, HA and M1 by flow cytometry. (A) Representative flow plots for mock- and
908 WSN-infected cells are shown. Gates for positive cell populations were set in
909 comparison to mock-infected cells. Due to differences in the side scatter (SSC)
910 profile between dTHP1 cells and MDM, the Y-axis (SSC) range is different
911 between the two cell types. (B) Percentages of cells positive for vRNP, HA, and
912 M1 are compared between dTHP1 and MDM. (C) MFIs (normalized to dTHP1
913 cells) for all three viral components are shown for positive cell populations (gated
914 in panel A). Data are from at least three independent experiments and are shown
915 as mean +/- SD. ns, non-significant.

916

917 **Supplementary Figure 3: Majority of NA-expressing dTHP1 cells and MDM**
918 **co-express both HA and M2.** dTHP1 cells and MDM were infected with WSN at
919 MOI 0.1 for 16 hours. Cells were fixed and stained for surface HA, M2, and NA.
920 Representative plots are shown in the left panel. % cells expressing HA and M2
921 within the NA-positive cell population were determined and shown in the right
922 panel. Data are from at least three independent experiments and shown as mean
923 +/- SD. ns, non-significant.
924
925 **Supplementary Figure 4: Cytochalasin D treatment does not increase cell**
926 **surface expression of HA, NA, and M2 in dTHP1 cells and MDM.** dTHP1 cells
927 and MDM were infected with WSN at MOI 0.1 for 14 hours. Cells were treated
928 with vehicle control (DMSO) or 20 μM Cyto D for 2 hours. (A) % cells expressing
929 HA, NA, and M2 on the cell surface are shown. (B) MFIs for the indicated
930 proteins in positive cell populations are shown. Data are from three experiments
931 and shown as mean +/- SD. *, $p<0.05$; **,$p<0.01$; ***$p<0.005$.
932
933 **Supplementary Methods:** Details of methods for virus infection and detection of
934 infection are described.

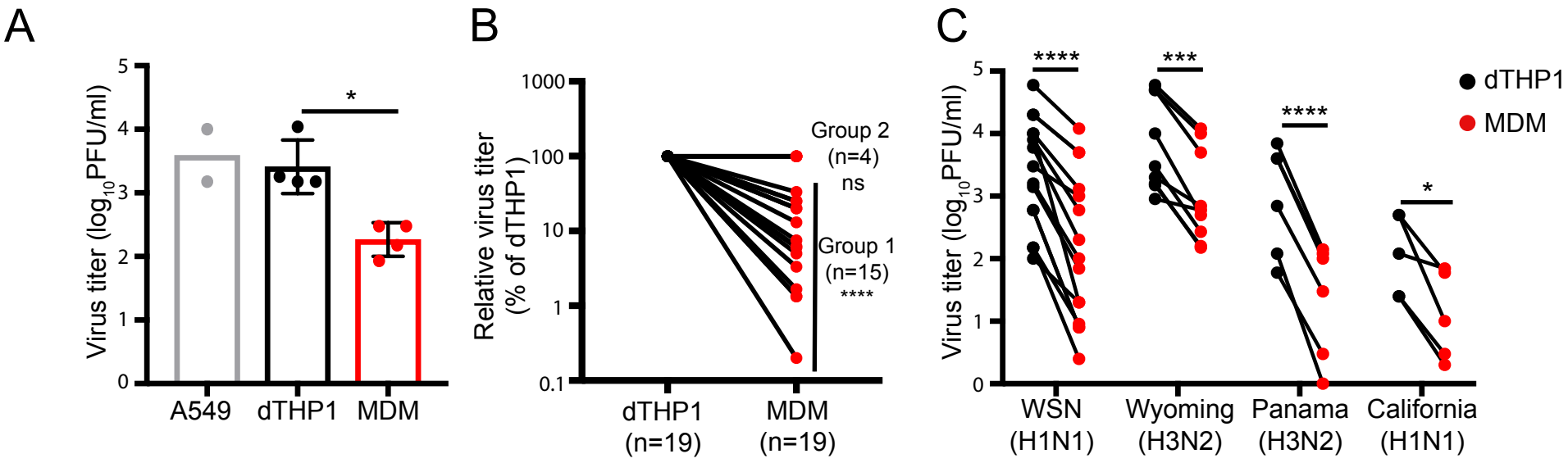

Figure 1: MDM are defective in productive IAV infection. (A) A549 cells, dTHP1 cells and MDM were infected with WSN at MOI 0.01. Infectious virus titers in culture supernatants were measured at 11 hpi. (B) Infectious virus titers in culture supernatants were measured for WSN-infected dTHP1 cells and MDM at 24 hpi. For all tested donors, the relative virus titers in MDM cultures were calculated in comparison to the titer in dTHP1 cell cultures tested in parallel within the same experiment. Two groups of donors (Groups 1 and 2) were denoted based on the reduction in the titers or lack thereof. (C) dTHP1 and MDM (Group 1) were infected with the given IAV strains at MOI 0.01, and infectious virus titers in culture supernatants were measured at 24 hpi. Each circle represents an independently prepared culture. A black and a red circle connected by a line represent each independent experiment. For panel A, data are shown as mean +/- SD. *, P<0.05; ***, P<0.001; ****, P<0.0001; ns, non-significant.

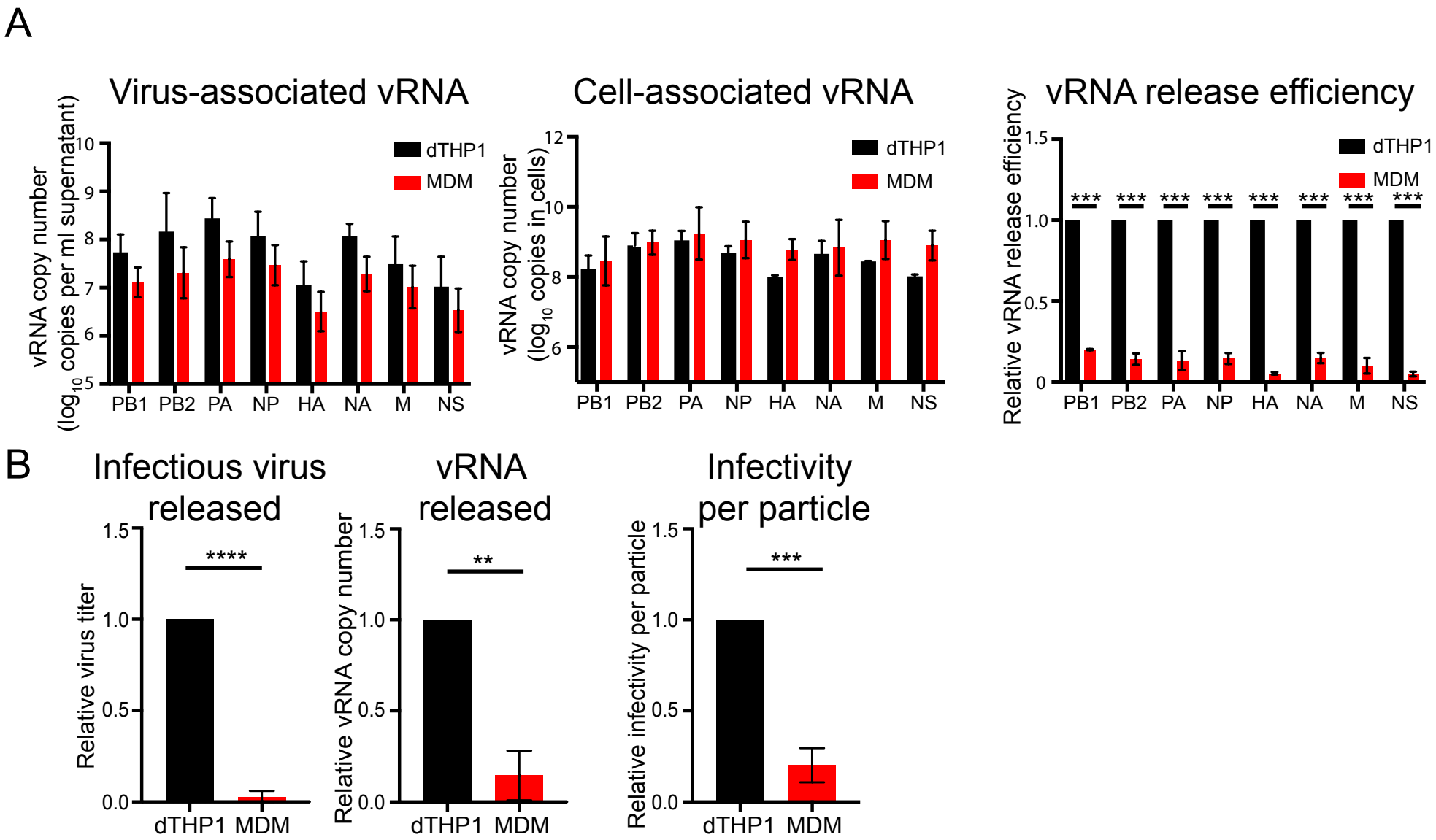

Figure 2: Both efficiency of virus release and infectivity of released particles are reduced in MDM than in dTHP1 cells. dTHP1 cells and MDM were infected with WSN at MOI 0.1. (A) vRNA copy numbers were measured in lysates of virus pelleted from cell culture supernatants and cell lysates at 20 hpi. vRNA release efficiency was calculated as the ratio of number of vRNA copies in virus lysates versus total number of vRNA copies (cell + virus) for each vRNA segment. (B) PB2 vRNA copy number and virus titer were measured in dTHP1 and MDM culture supernatants at 16 hpi. Infectivity per particle was calculated as the ratio of virus titer to PB2 vRNA copy number in culture supernatants. Data are from experiments done with MDM from at least three independent donors and shown as mean +/- S.D. **, P<0.01; ***, P<0.001, ****, P<0.0001.

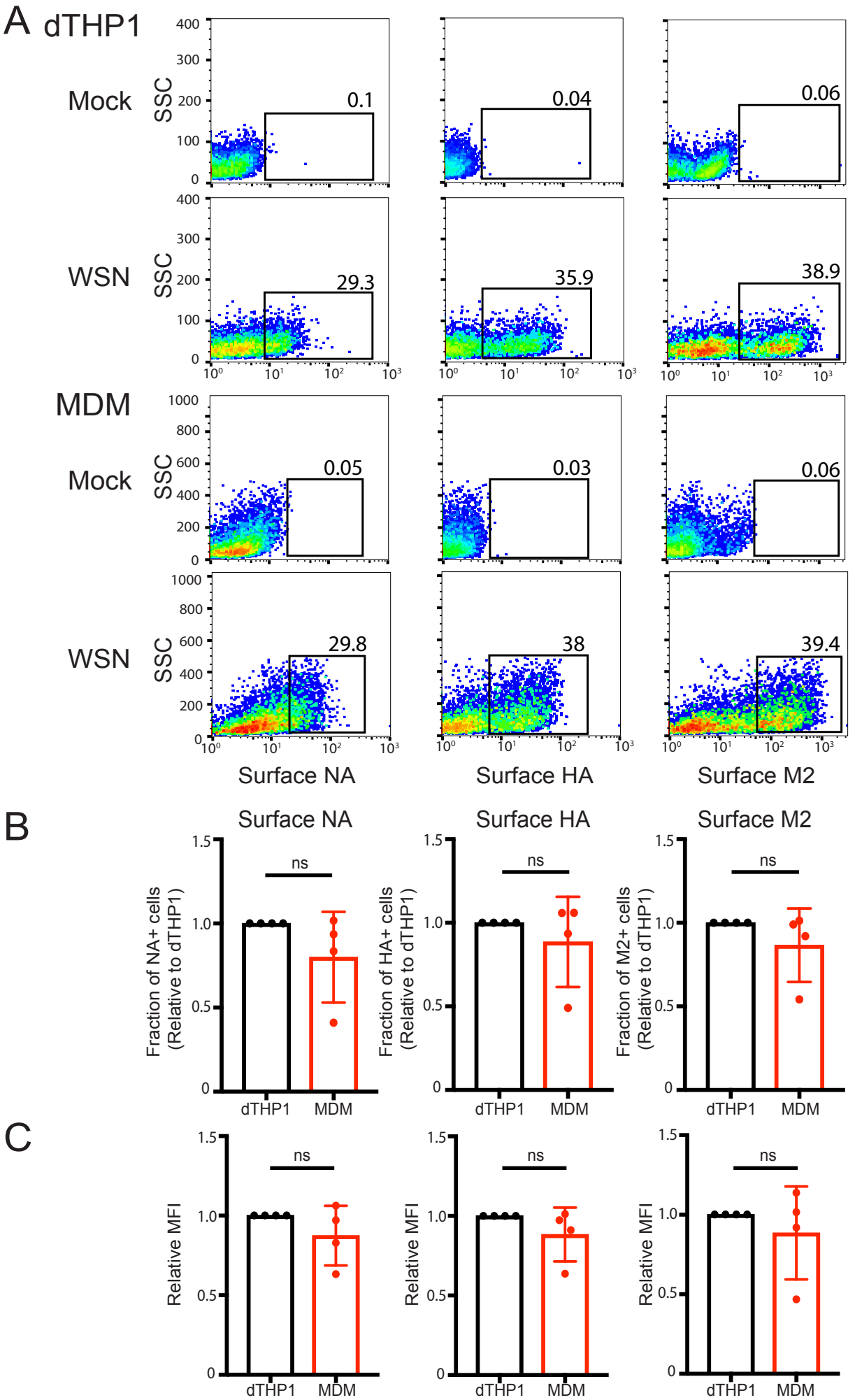
A
dTHP1
Mock
WSN
MDM
Mock
WSN
SSC
0.1
0.04
0.06
29.3
35.9
38.9
0.05
0.03
0.06
29.8
38
39.4
Surface NA
Surface HA
Surface M2
B
Surface NA
Surface HA
Surface M2
Fraction of NA+ cells (Relative to dTHP1)
Fraction of HA+ cells (Relative to dTHP1)
Fraction of M2+ cells (Relative to dTHP1)
ns
dTHP1
MDM
C
Relative MFI
ns
dTHP1
MDM

Figure 3: MDM are efficient at trafficking of viral glycoproteins to the cell surface. dTHP1 cells and MDM were infected with WSN at MOI 0.1. (A) Infected cells were analyzed for cell surface expression of HA, NA, and M2 by flow cytometry at 16 hpi. Representative flow plots for mock-infected (top row) and virus-infected (bottom row) cells are shown. Percentages of cells positive for viral proteins (boxed) are shown. Due to differences in the side scatter (SSC) profile between dTHP1 cells and MDM, the Y-axis (SSC) range is different between the two cell types. (B) Percentages of cells positive for surface expression of NA, HA, and M2 are compared between dTHP1 and MDM. (C) Relative MFIs for surface signal of indicated proteins for positive cell populations (gated in panel A) are shown. Data are shown as mean +/- SD and are from at least three independent experiments. ns, non-significant.

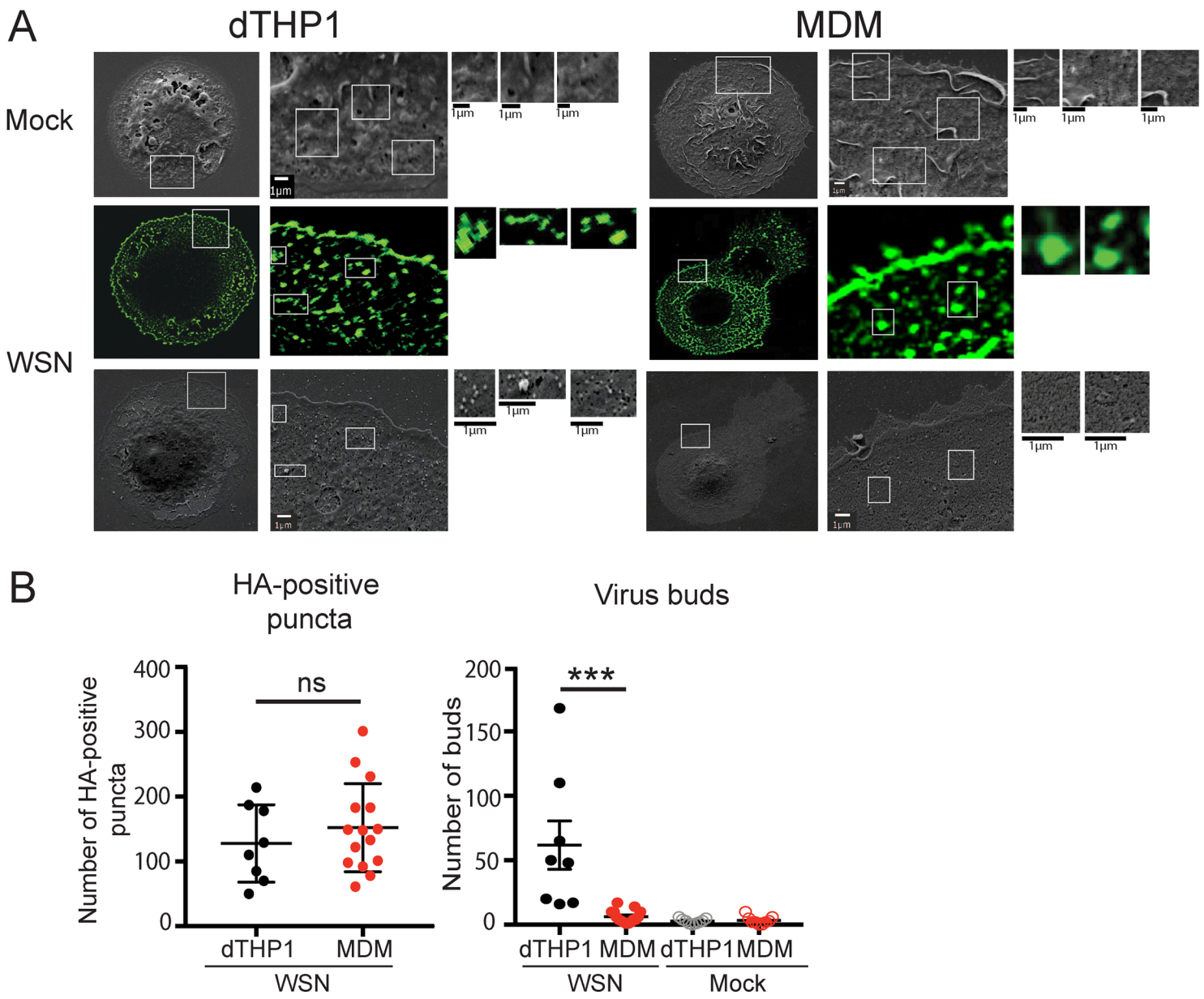

Figure 4: MDM are defective in virus bud formation despite expression of HA on the cell surface. dTHP1 cells and MDM grown on gridded coverslips were infected with WSN at MOI 0.1 for 20 hours. Cells were fixed and immunostained with anti-HA. After identification of HA-positive cells by confocal microscopy, cells were prepared for SEM. The same cells were identified based on grid positions and analyzed by SEM. (A) Representative SEM images for mock-infected and WSN-infected HA-positive cells are shown in the top and bottom rows, respectively. Fluorescence images corresponding to the SEM images of WSN-infected cells are shown in the middle row. Boxed areas are magnified and shown in the right panels. (B) The number of HA-positive puncta identified in fluorescence images (left panel) and ~100-nm buds identified in SEM images (right panel) were counted within the same area (100 µm2 in size) in each cell. Data are shown for 8-15 cells from two independent experiments. Error bars represent SEM. ***, P<0.0001; ns, non-significant.

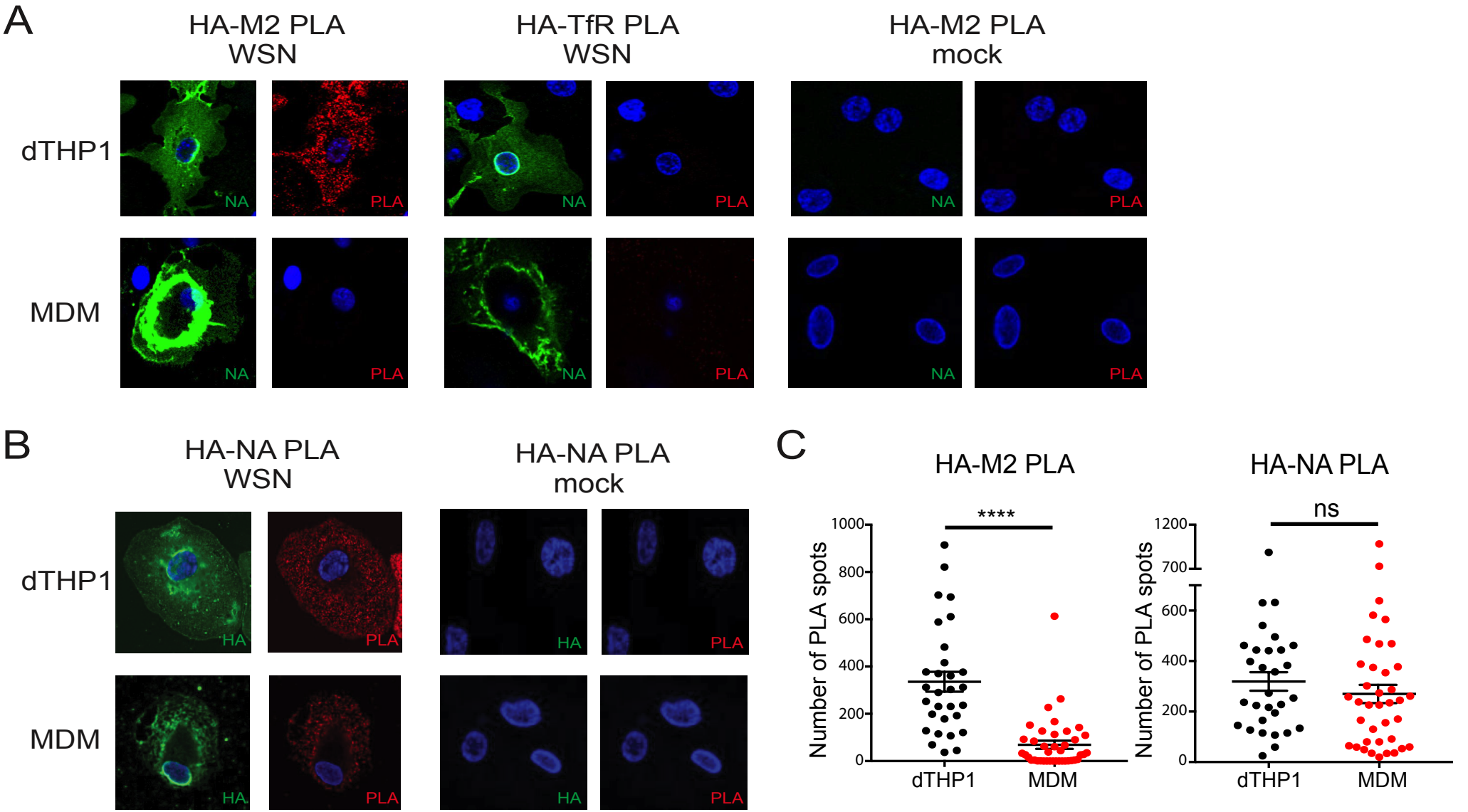

Figure 5: Association between HA and M2 is defective in MDM relative to dTHP1 cells. dTHP1 cells and MDM were infected with WSN at MOI 0.1 for 16 hours. (A) Cells were examined by PLA using goat anti-HA and mouse anti-M2 or goat anti-HA and mouse anti-TfR antibodies. To identify infected cells, surface NA was also detected by rabbit anti-NA. Nuclei were stained with DAPI (blue). Representative maximum intensity projection images, which were reconstructed from z-stacks corresponding to the focal planes ranging from the middle plane of the nucleus to the bottom of the cells, are shown. (B) Cells were examined by PLA using mouse anti-HA and rabbit anti-NA antibodies. Goat anti-HA was used for detection of infected cells. Representative maximum intensity projection images are shown as in panel A. Note regions of intense NA (in A) and HA (in B) signal on the surface of MDM due to the presence of membrane ruffles. (C) Number of PLA spots were counted for each cell. Data are shown for three independent experiments, and 8-10 cells were analyzed per experiment. These experiments were performed in parallel with the experiments shown in Figure 3 using MDM from the same donors. Error bars represent SEM. *, $p<0.05$; ****, $p<0.0001$; ns, non-significant.

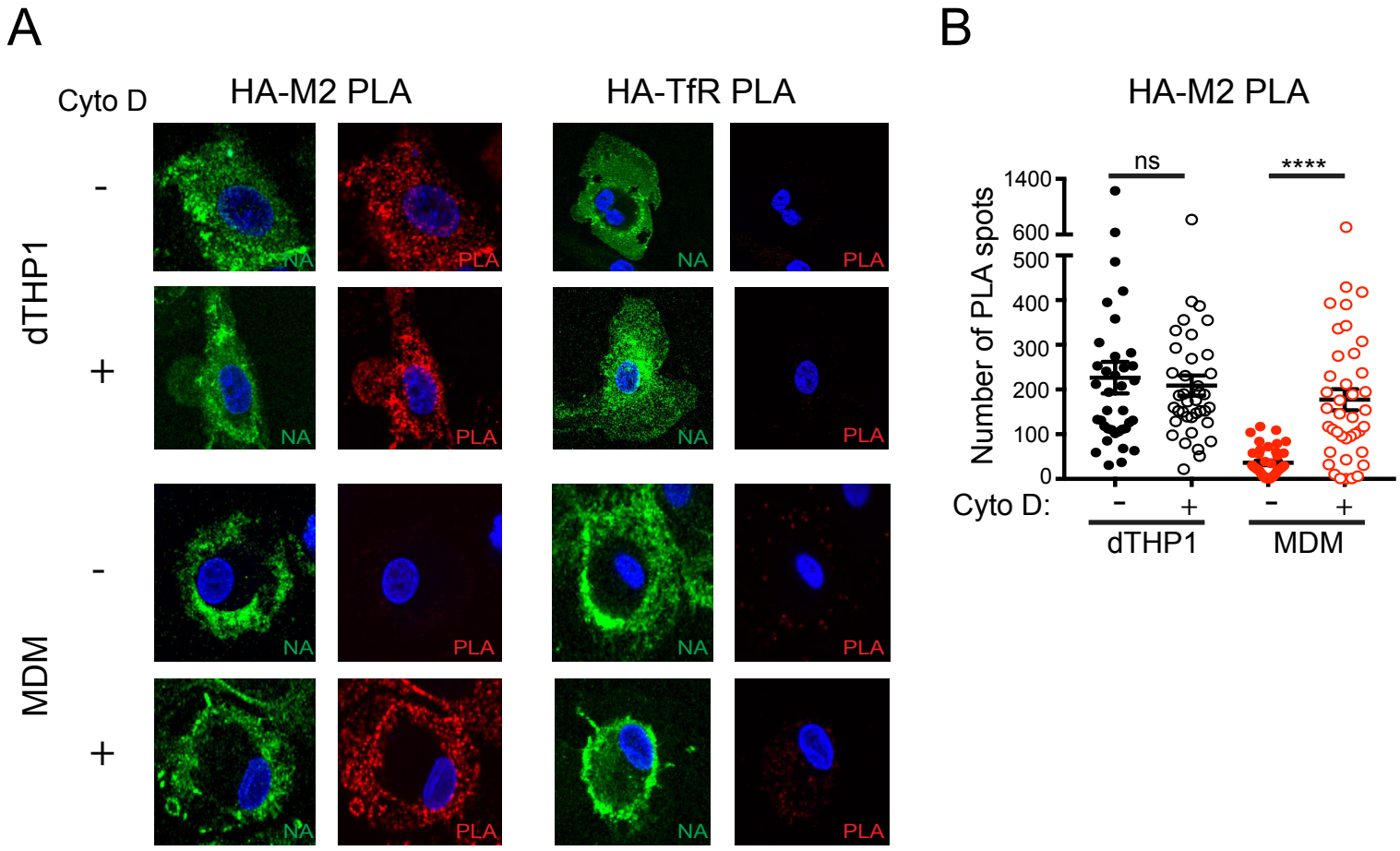

Figure 6: Cytochalasin D treatment restores HA-M2 PLA in MDM to levels comparable to that in dTHP1 cells. dTHP1 cells and MDM were infected with WSN at MOI 0.1. At 14 hpi, cells were treated with vehicle control (DMSO) or 20 μM cytochalasin D (Cyto D) for 2 hours before fixation. (A) Cells were analyzed as in Figure 5A. Representative maximum intensity projection images are shown. (B) Number of PLA spots were counted for each cell. These experiments were performed in parallel with the experiments shown in Supplementary Figure 4 using MDMs from the same donors. Data are from at least three independent experiments, and 8-10 cells were analyzed per experiment. Error bars represent SEM. ****, $p < 0.0001$; ns, non-significant.

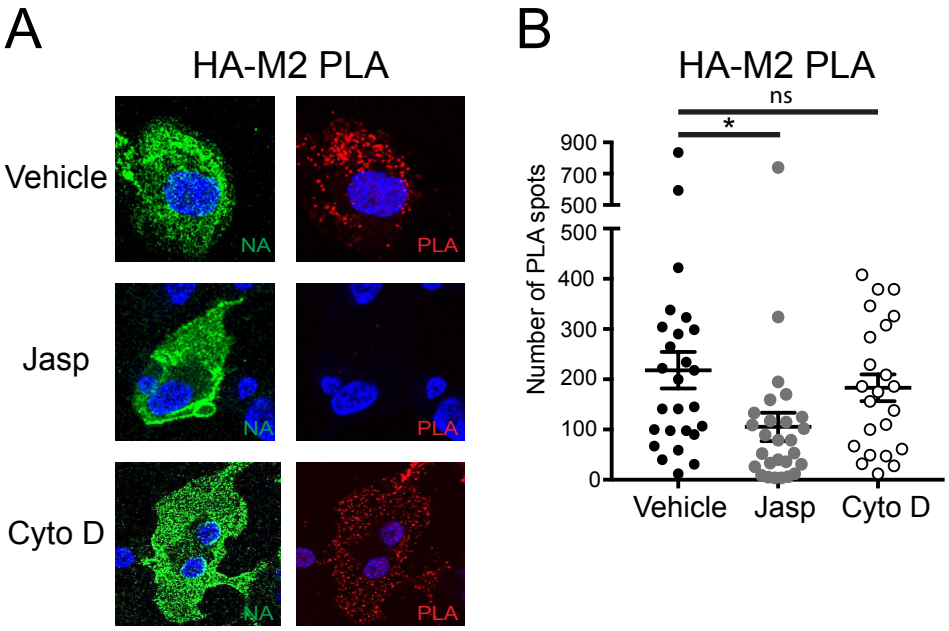

Figure 7: Jasplakinolide treatment reduces HA-M2 PLA in dTHP1 cells. dTHP1 cells were infected with WSN at MOI 0.1. At 10 hpi, cells were treated with vehicle control (100% Ethanol), 1 μM Jasplakinolide (Jasp), or 20 μM Cyto D for 4 hours before fixation. (A) Representative maximum intensity projection images are shown as in Figure 5A. (B) Number of PLA spots were counted for each cell. Data are from at least three independent experiments, and 7-10 cells were analyzed per experiment. Error bars represent SEM. *, $p < 0.05$; ns, non-significant.

Supplementary Methods

Virus infection: For virus infection, cells were first washed twice with MEM-BSA medium (1X MEM supplemented with 0.3% BSA (Sigma), 0.23% sodium bicarbonate (Gibco), 1X MEM amino acids (Gibco), and 1X MEM vitamins (Gibco)). The cells were then inoculated with diluted virus at MOI 0.01 or 0.1 for 1 hour at 37°C, washed twice with MEM-BSA, and cultured in MEM-BSA containing 0.2 µg/ml tosylsulfonyl phenylalanyl chloromethyl ketone (TPCK)-treated trypsin (Worthington).

Infectious virus measurement by plaque assay: Confluent monolayers of MDCK cells (cultured up to passage 40) plated in 24-well plates were washed twice with MEM-BSA and incubated with 100 µl of serial dilutions of virus supernatants for 1 hour at 37°C. Cells were washed once with MEM-BSA and layered with MEM-BSA containing 0.76 ug/ml TPCK-treated trypsin and 1% Seakem GTG agarose /Seaplaque (Lonza). After gelation of agarose, the plates were inverted and incubated at 37°C. After 48-72 hours, the agarose was removed, and the cells were stained with crystal violet (0.1% crystal violet in 20% methanol) for 10 minutes before counting plaques.

Flow cytometry: For viral protein expression analysis by flow cytometry, virus- or mock-infected cells were detached using 0.06% trypsin-EDTA in phosphate-buffered saline (PBS) and fixed with 4% paraformaldehyde (PFA, Electron

Microscopy Sciences) in PBS for 20 minutes at room temperature. After fixation, cells were washed twice with 2% FBS in PBS (FACS buffer). For detecting viral protein expression on the cell surface, cells were subsequently incubated with primary antibodies for 45-60 minutes directly. For staining of intracellular proteins, cells were first permeabilized with 0.1% TritonX-100 in PBS for 5 minutes and then probed with primary antibodies. After washing once with the FACS buffer, cells were incubated with fluorescently labeled secondary antibodies (Invitrogen) for 20-30 minutes. Cells were washed twice with the FACS buffer and analyzed using the FACSCanto flow cytometer (BD Biosciences). Data were analyzed in FlowJo (Treestar), and the positive gates were set using the mock-infected controls.

Primers for vRNA measurement

The following primers were used for detection of vRNAs:

PB1 forward: 5'-TCAGAGAAAGAGACGAGTGAG-3', PB1 reverse: 5'-AAACCCCCTTATTTGCATCC-3'

PB2 forward: 5'- GTTGGGAGAAGAGCAACAGC-3', PB2 reverse: 5'-GATTCGCCCTATTGACGAAA-3'

PA forward: 5'- TGTGCAGCAATGGATGATTT-3', PA reverse: 5'-TCTCCCATTTGTGTGGTTCA-3'

NP forward: 5'- GCGCCAAGCTAATAATGGTG-3', NP reverse: 5'-GGAGTGCCAGATCATCATGT-3'

M forward: 5’-GACCRATCCTGTCACCTCTGAC-3’, M reverse: 5’-AGGGCATTYTGGACAAAKCGTCTA-3’

NS forward: 5’- CAGAATGGACCAGGCGATCA-3’, NS reverse: 5’-TAGAGTCTCCAGCCGGTCAA-3’

HA forward: 5’-TAACCTGCTCGAAGACAGAC-3’, HA reverse: 5’-AGAGCCATCCGGTGATGTTA-3’

NA forward: 5’- TTGGTCAGCAAGTGCATGTC-3’, NA reverse: 5’-ACAGCCACTGCTCCATCATC-3’.

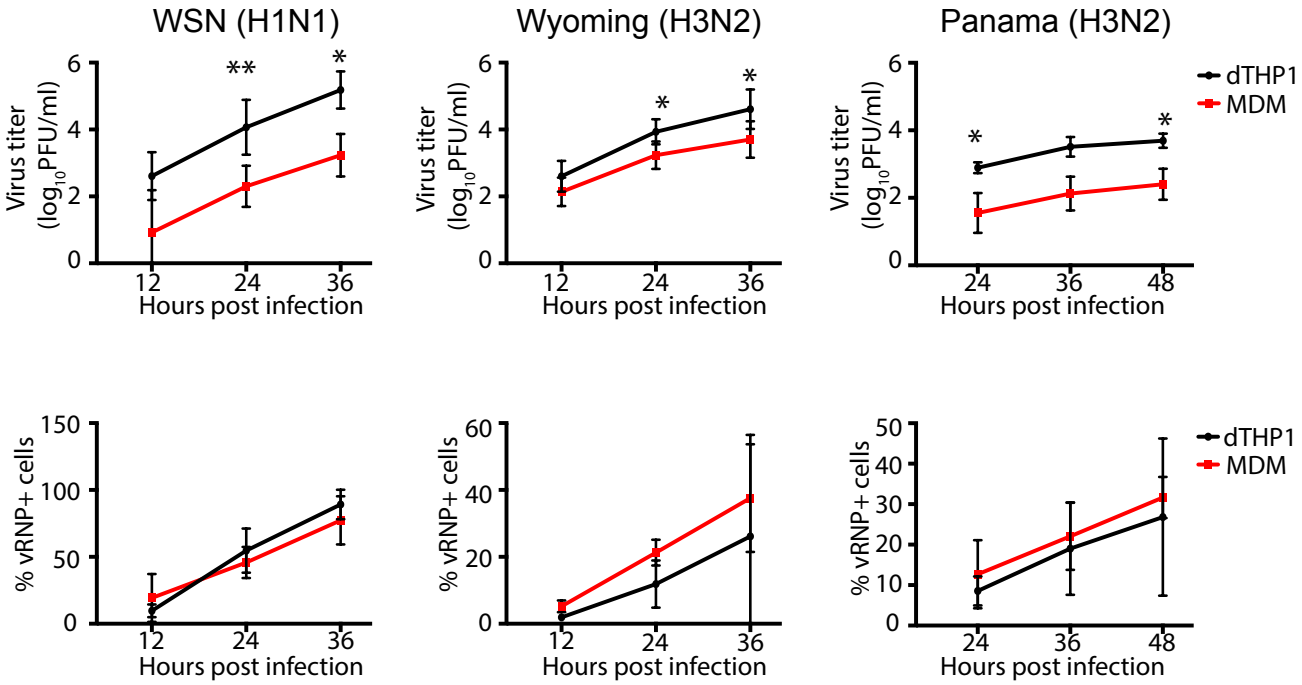

Supplementary Figure 1

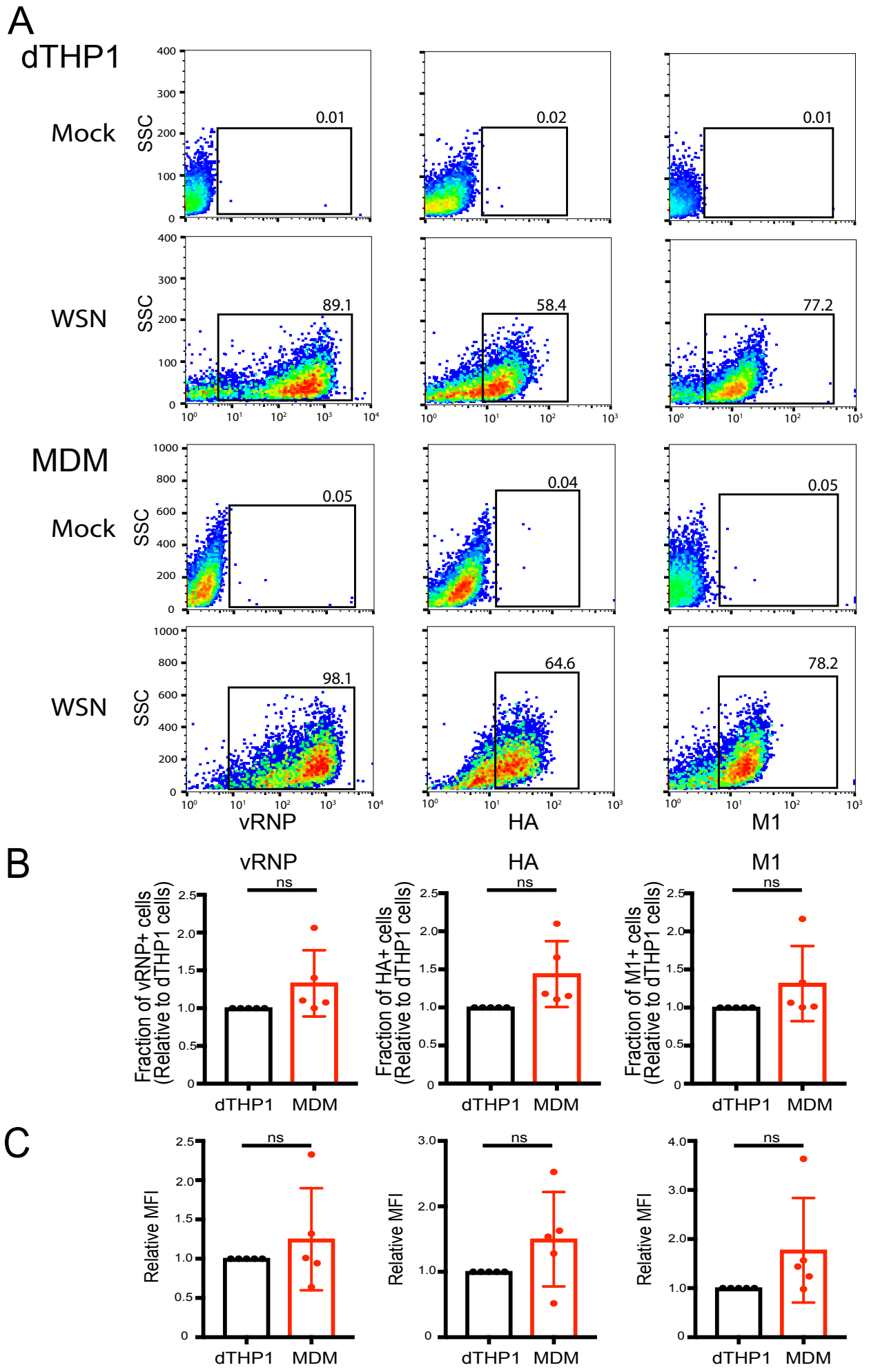

Supplementary Figure 2

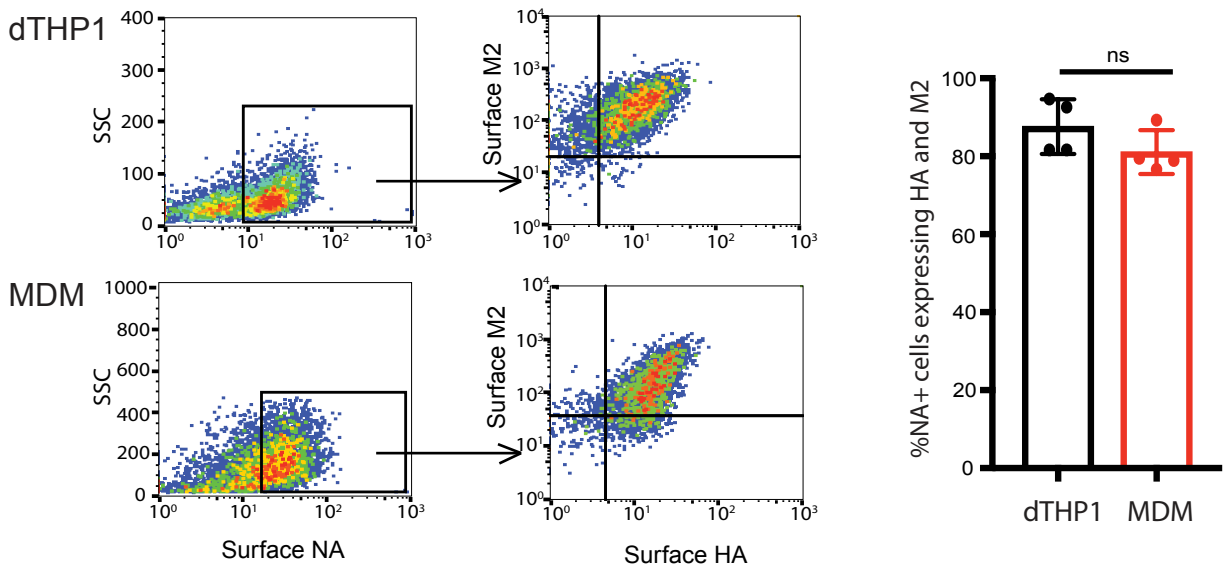

Supplementary Figure 3

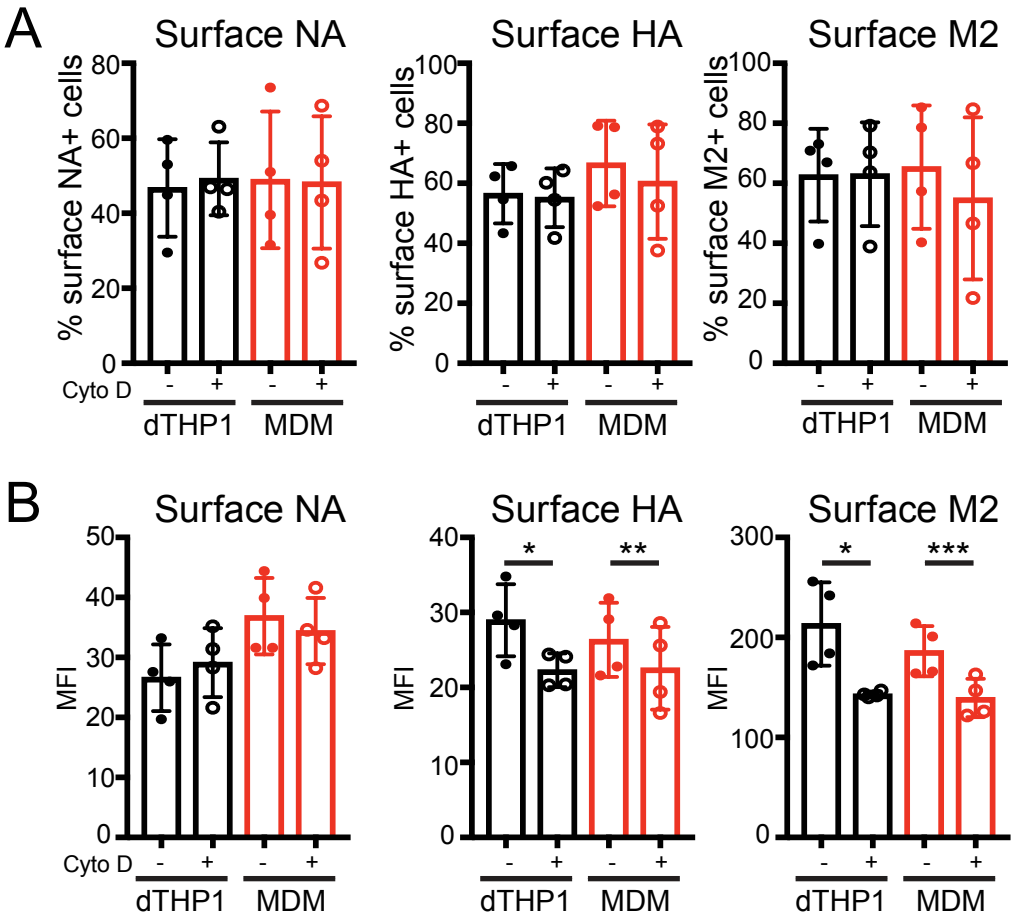

Supplementary Figure 4